CR-152,008

(NASA-CR-152008) STUDY OF A HIGH PERFORMANCE EVAPORATIVE HEAT TRANSFER SURFACE Final Report (Sigma Research, Inc., Richland, Wash.) 82 p HC A05/MF A01 CSCL 20D G3/34

N78-10411

Unclas 45625

SIGMA RESEARCH, INC.
2950 GEORGE WASHINGTON WAY
RICHLAND WASHINGTON 99352

STUDY OF A HIGH PERFORMANCE EVAPORATIVE HEAT TRANSFER SURFACE

by

ELRIC W. SAASKI

and

R. H. HAMASAKI

May 27, 1977

Prepared for

Ames Research Center
National Aeronautics and Space Administration
Moffett Field, California 94035

CR-152,008

FINAL REPORT

on

STUDY OF A HIGH PERFORMANCE EVAPORATIVE HEAT TRANSFER SURFACE

NAS2-9120

by

ELRIC W. SAASKI

and

R. H. HAMASAKI

May 27, 1977

SIGMA RESEARCH, INC.
2950 George Washington Way
Richland, Washington 99352

ABSTRACT

An evaporative surface is described for heat pipes and other two-phase heat transfer applications that consists of a hybrid composition of V-grooves and capillary wicking. Characteristics of the surface include both a high heat transfer coefficient and high heat flux capability relative to conventional open-faced screw thread surfaces. With a groove density of 12.6 cm^{-1} and ammonia working fluid, heat transfer coefficients in the range of 1 to 2 W/cm^2K have been measured along with maximum heat flux densities in excess of 20 W/cm^2. A peak heat transfer coefficient in excess of 2.3 W/cm^2K was measured with a 37.8 cm^{-1} hybrid surface.

TABLE OF CONTENTS

LIST OF FIGURES

LIST OF FIGURES (continued)

NOMENCLATURE

a = constant heat flux zone height, cm
A_g = cross-sectional area of single groove opening, cm^2
b = bar height (Figure 2.3-1), cm
c = friction factor coefficient (Table 2-1)
d = local film thickness (Figure 5-2), cm
D_h = hydraulic diameter of groove cross-section, cm
$F_{v\ell}$ = laminar friction factor
g = gravitational acceleration, cm/sec^2
G_ℓ = fillet conductance, W/cmK
h_{fg} = latent heat of vaporization, ergs/gm
H = evaporative heat transfer coefficient, W/cm^2K
$\bar{H}$ = effective value of local film coefficient, W/cm^2K
H_i = local interfacial heat transfer coefficient, W/cm^2K
$K_{w,\ell}$ = wall and liquid thermal conductivity, respectively, W/cmK
K_{pw} = capillary wick permeability, cm^2
L = distance between vapor vent slots, cm
M = working fluid molecular weight, gm/g-mole
N = groove linear density, cm^{-1}
P = covered groove perimeter, viewed in cross-section, cm
P^+ = ratio of differential vapor pressure to surface tension pressure
P_b = total pressure within vapor bubble, $dynes/cm^2$
P_ℓ = liquid phase pressure, $dynes/cm^2$
P_{sd} = saturated vapor pressure corresponding to T_{sd}, $dynes/cm^2$
P_{sr} = saturated vapor pressure corresponding to T_{sr}, $dynes/cm^2$
P_v = vapor pressure within covered groove, $dynes/cm^2$
P_{vs} = heat pipe vapor core pressure, $dynes/cm^2$
P_δ = vapor pressure at liquid film surface, $dynes/cm^2$
q_a = evaporative heat flux density, W/cm^2
q_{am} = maximum evaporative heat flux density, W/cm^2
q_ℓ = heat flux per unit length of fillet, W/cm
Q_a = local heat flux density at meniscus-vapor interface, W/cm^2

r = local film radius of curvature, cm

r_b = vapor bubble radius, cm

r_{bi} = vapor bubble departure radius from site with radius r_{ni}, cm

r_{cw} = capillary pore radius for wick material covering grooves, cm

r_{ni} = critical nucleation site radius such that $P^+ = 1$, cm

r^+_{ni} = r_{ni}/d

R = radius of inscribed circle (Figure 2.1-1), cm

Re = Reynolds number

R_{th} = thermal constriction resistance, cm^oC/W

t = capillary wick thickness, cm

T = local wall temperature (Section 2.4), K

T_m = mean liquid-vapor interfacial temperature, K

T_v = vapor phase temperature = T_{vs}, K

T_δ = liquid film surface temperature, K

T_w = local wall temperature, K

T_o = constant temperature at fin root, K

$T_{\ell r}$ = liquid temperature at $y = r$, K

T_{sd} = film surface temperature (saturated conditions assumed), K

T_{sr} = liquid temperature at $y = r$, K

T_{vs} = saturation temperature corresponding to P_{vs}, K

T_{we} = exterior evaporator wall temperature, K

U_1 = liquid film surface velocity, cm/sec

U_{av} = average vapor velocity in groove, cm/sec

V_{fg} = volumetric change per gram in vaporization, cm^3/gm

w = fin half-width (Figures 2.3-1 and 2.4-1), cm

w_a = land width (Figure 3-2), cm

w_b = groove width (Figure 3-2), cm

We = Weber number

X = coordinate defined in Figure 2.2-1

Y_f = final height of vapor bubble if bubble can grow from initial nucleation radius r_{ni}, cm

α = defined by Equation 5-7b

β = fraction of local film thickness penetrated by vapor bubble, cm

δ = local film thickness (equivalent to "d"), cm

$\Delta\dot{m}$ = differential mass arrival rate at meniscus-vapor interface, gm/cm^2sec

$\Delta P_{\ell m}$ = maximum liquid phase pressure drop relative to heat pipe vapor, $dynes/cm^2$

$\Delta P_{\ell o}$ = liquid phase pressure drop up to position $X = \frac{L}{2}$, relative to heat pipe vapor core, $dynes/cm^2$

ΔP_{vm} = maximum vapor pressure rise in covered groove relative to heat pipe vapor core, $dynes/cm^2$

$\Delta P_{\ell vm}$ = maximum liquid-vapor pressure difference, $dynes/cm^2$

η = $\Delta P_{vm}/\Delta P_{\ell m}$

$\nu_{\ell,v}$ = liquid and vapor kinematic viscosities, cm^2/sec

θ = total groove angle, radians

λ = characteristic dimension of surface disturbance, cm

$\mu_{\ell,v}$ = liquid and vapor phase viscosities, respectively, poise

$\rho_{\ell,v}$ = liquid and vapor phase densities, respectively, gm/cm^3

σ = surface tension, dynes/cm

ϕ = wall superheat factor defined by Equation 5-5, cm

ϕ_{ni} = value of ϕ corresponding to $P^+ = 1$, cm

ϕ_{yf} = superheat factor corresponding to a bubble of height $y = y_f$, cm

1.0 INTRODUCTION

The development of methods for reducing the interfacial thermal resistance between a solid surface and a contacting liquid is an area of significant engineering and economic importance. One of the most effective techniques used is two-phase heat transfer which is characterized by a liquid-to-vapor transition at or near the solid surface. There are basically two methods of two-phase heat transfer, and this distinction relates to the predominant energy-carrying species. In boiling heat transfer, vapor bubbles generated at the surface create a turbulent mixing and pumping phenomenon that circulates unheated liquid from the bulk fluid into a position near the heated wall, and it is the sensible heat capacity in this colder liquid that, in most cases, dominates heat removal. In film evaporation, on the other hand, the surface is oriented or structured to minimize liquid film thicknesses, and heat removal is dominated by thermal conduction through the film and vaporization from the film surface. The heat pipe is a prime example of a device relying on film heat transfer. To minimize the film conduction temperature drop while maintaining uniform surface wetting, heat pipes have employed thin capillary wick surface coverings and grooves cut or extruded into the heat pipe wall. Over the past several years, capillary wick surfaces have gradually lost favor because the grooved surfaces provide more reproducible performance and can be produced at low cost using extrusion or threading processes for groove densities less than about 50 cm^{-1}. In addition, with groove densities on the order of 60 cm^{-1}, heat transfer coefficients up to 2 W/cm^2K have been measured with ammonia working fluid.[1] Pool boiling of ammonia, in comparison, shows a heat transfer coefficient on the order of 0.4 to 1.0 W/cm^2K in the heat flux density range 1 to 10 W/cm^2.[2] For terrestrial applications, boiling heat transfer can be used in heat pipes, but for space applications, boiling in zero-g appears to produce a large vapor blanket around the heated object which severely limits heat transfer.[3]

Disadvantages of grooved surfaces for film heat transfer include poor capillary pumping capability and fabrication difficulties when more than 50 grooves/cm are desired. A grooved surface has a periodic liquid film structure with

a principal radius of curvature equal to approximately one-half the groove width, while a capillary wick has two principal radii of curvature. For the same characteristic liquid fillet dimension, a capillary wick will pump twice the static head or twice the heat flux (assuming identical axial heat pipe fluid return conductances).

High groove densities are desired because it is commonly held that the majority of heat transfer occurs over a relatively short zone where the liquid meniscus attaches to the groove.[4-6] When conventional machining processes are used to produce over 50 grooves/cm, difficulties arise in uniformity of groove shape and depth, chip removal, and tool wear. In the production of axial grooves, a similar limit occurs in the range of 40 grooves/cm.[7]

The hybrid surface to be discussed here is a combination of capillary wick and grooves that possesses the pumping capability of the capillary wick along with the high heat transfer coefficient of fillet evaporation.

2.0 ANALYSIS

2.1 Description

A cross-sectional view of the evaporative surface is presented in Figure 2.1-1a, while Figure 2.1-1b shows a corresponding section through a V-groove surface. The hybrid surface, which has been coined the "inverted meniscus wick," is produced by covering the V-grooves with a fine-pored capillary screen or felt-metal. The capillary material does not cover the entire surface, however. The covering is periodically vented perpendicular to the groove axes to allow the grooves to communicate with the general vapor space. Prior to heat addition, the capillary wick and grooves will be primed with liquid, but when the metal substrate is heated, liquid will recede into the groove because of wick pressure drops and perhaps as a result of boiling caused by wall superheat. The resulting liquid/vapor structure will be similar to that shown in Figure 2.1-1a, with an inverted liquid meniscus and a tear-drop shaped vapor microchannel. Vapor generated through thin-film evaporation from the fillet structure passes down the vapor microchannel and is exhausted into the general vapor space through one of the periodic vent slots. In contrast to open groove surfaces, allowable fillet recession is now totally independent of groove size and shape, and instead, is tied to liquid pressure drops and capillary wick pore size. Application of this evaporative wick to a cylindrical spiral groove evaporator is shown in Figure 3-3. In this case, capillary screen wick was wrapped on a steel mandrel, and the mandrel and wick were then inserted into the grooved tube. Vapor generated under the screen cover traveled a circumferential path in the array of spiral grooves, and was discharged into the general heat pipe vapor core through two axial slots in the mandrel.

As depicted in this figure, the inverted meniscus wick is more complex than the open groove evaporator, and perhaps more costly (although attention has not been specifically directed towards mechanical design optimization). Experimental tests described in a later section show the inverted meniscus possesses very high heat transfer coefficients and maximum heat flux densities,

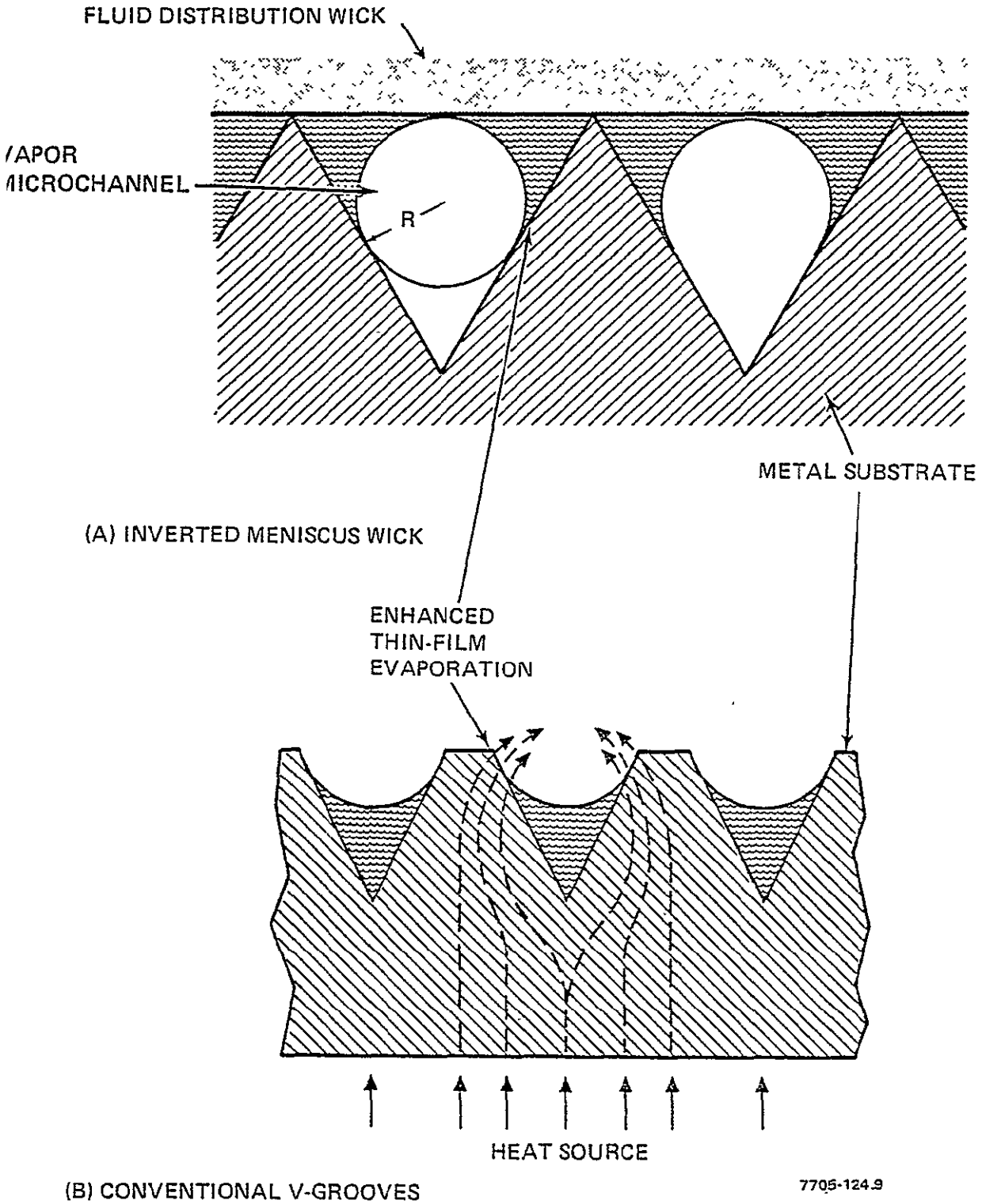

FIGURE 2.1-1. A COMPARISON OF THE INVERTED MENISCUS WICK WITH A CONVENTIONAL V-GROOVE SURFACE

and these attributes must be balanced against the increased surface complexity to determine whether the inverted meniscus surface is appropriate for a specific application.

2.2 Operating Constraints

Liquid and Vapor Pressure Drops

The operating limits of an inverted meniscus evaporator deal primarily with hydrodynamic pressure drops, and particularly with ensuring that the vapor phase pressure drop in the groove does not exceed capillary wick pumping capability. In a previous report,[8] pressure drop constraints were derived for V-groove surfaces. In this section, that analysis will be broadened to include grooves of arbitrary shape.

Figure 2.2-1 illustrates two fundamental vapor-liquid flow geometries for the inverted meniscus. The vapor slots are shown spaced a distance "L" apart. In Figure 2.2-1a, the flow of liquid and vapor are counter-current, while in Figure 2.2-1b, the liquid and vapor flows are co-current. The first condition corresponds to a situation where the vapor exhaust slots at $X = \pm L/2$ coincide with the points of liquid introduction, while the second condition corresponds to a situation in which liquid is introduced at the mid-point, $X = 0$. For condition -1a, it is apparent that the maximum vapor/liquid pressure difference occurs at $X = 0$, and is the algebraic sum of the liquid pressure change in the capillary wick and the vapor pressure change in a vapor microchannel. The liquid pressure contribution is

$$\Delta P_{\ell m} = \Delta P_{\ell o} + \frac{\mu_\ell L^2 q_a}{8K_{pw}\rho_\ell h_{fg} t} \qquad (\text{dynes/cm}^2) \qquad (2.2\text{-}1)$$

where $\Delta P_{\ell o}$ is the liquid-vapor pressure difference at $X = \pm\frac{L}{2}$, and where the common assumption of uniform evaporation per unit has been employed.

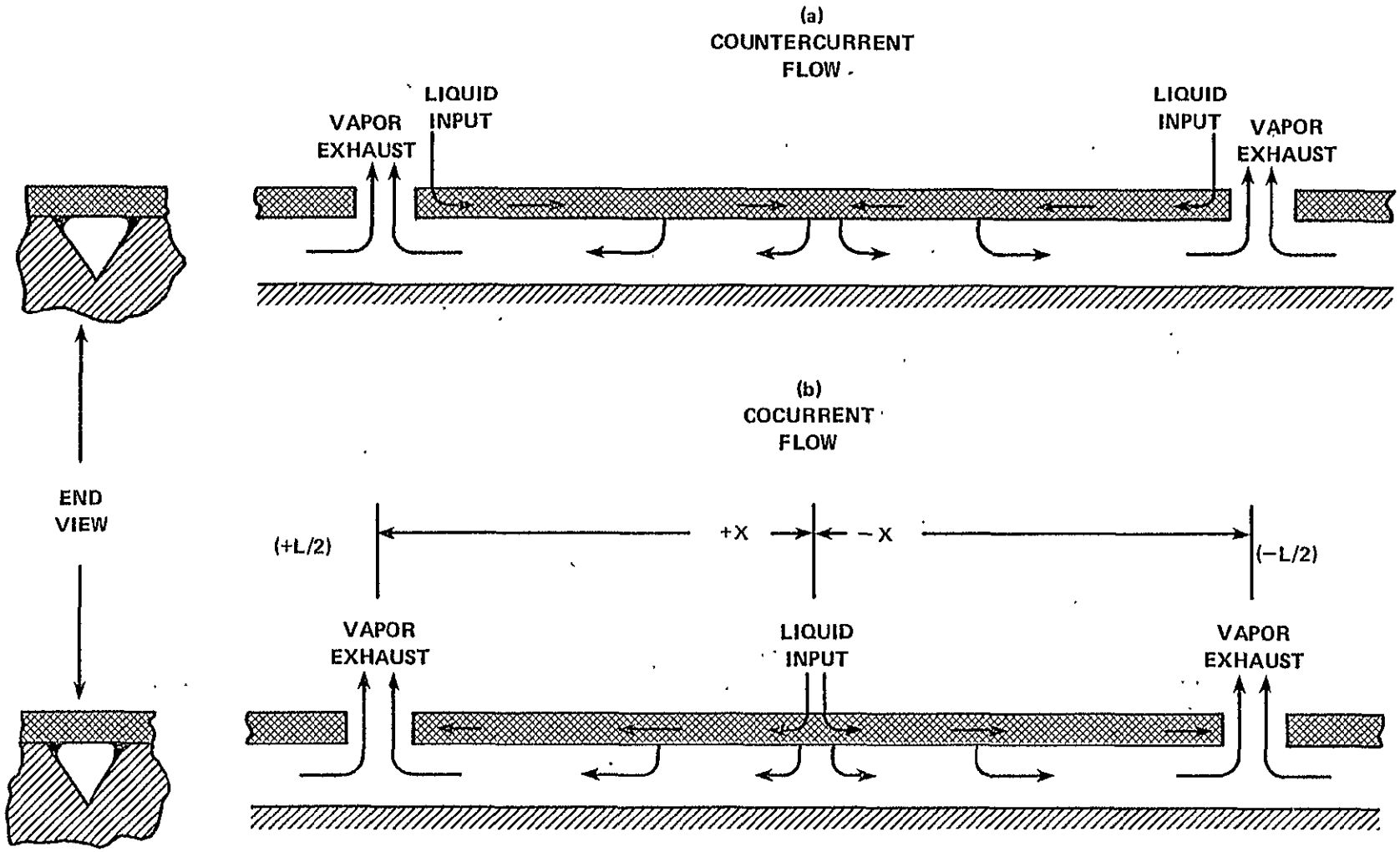

FIGURE 2.2-1. TWO ALTERNATE METHODS OF FEEDING LIQUID TO THE SURFACE WHICH RESULT IN COUNTERCURRENT AND COCURRENT LIQUID AND VAPOR FLOW AT THE EVAPORATOR WALL

7705-124.16

Estimation of the vapor phase pressure difference between X = 0 and either X = ±L/2 requires calculation of the microchannel hydraulic diameter D_h, and the cross-sectional area A_g. For laminar vapor flow and uniform evaporation per unit length of meniscus, the vapor pressure difference between the mid-point and the vapor release slot is given by

$$\Delta P_{vm} = \frac{c\,\mu_v L^2 q_a}{4\rho_v h_{fg} D_h^2 A_g N} \qquad \text{(dynes/cm}^2\text{)} \qquad (2.2\text{-}2)$$

Use of the following formula has been made:

$$F_{v\ell} = \frac{c}{Re} \qquad (2.2\text{-}3)$$

where $F_{v\ell}$ is the laminar friction factor, and the coefficient "c" is given in Table 2-1. For a triangular groove with total groove angle θ, the hydraulic diameter is

$$D_h = \frac{4A_g}{P} = \frac{W_b \cos(\theta/2)}{[1 + \sin(\theta/2)]} \qquad (2.2\text{-}4)$$

The total liquid-vapor pressure difference for configuration 2.2-1a is the sum of equations 2.2-1 and 2.2-2. For the special case that $\Delta P_{\ell o} = 0$, a maximum heat flux density q_{am} is defined on the basis of available capillary pumping pressure,

$$\frac{2\sigma}{r_{cw}} = \frac{q_{am} L^2 \mu_v}{8\rho_\ell h_{fg} t}\left[\frac{1}{K_{pw}} + 2\left(\frac{\nu_v}{\nu_\ell}\right)\frac{ct}{NA_g D_h^2}\right] \qquad (2.2\text{-}5)$$

The peak heat flux density q_{am} and corresponding vapor flow Reynolds number are shown in Figure 2.2-2 as a function of ammonia saturated vapor temperature for the experimental 37.8/cm grooved surface described in Section 3. In the

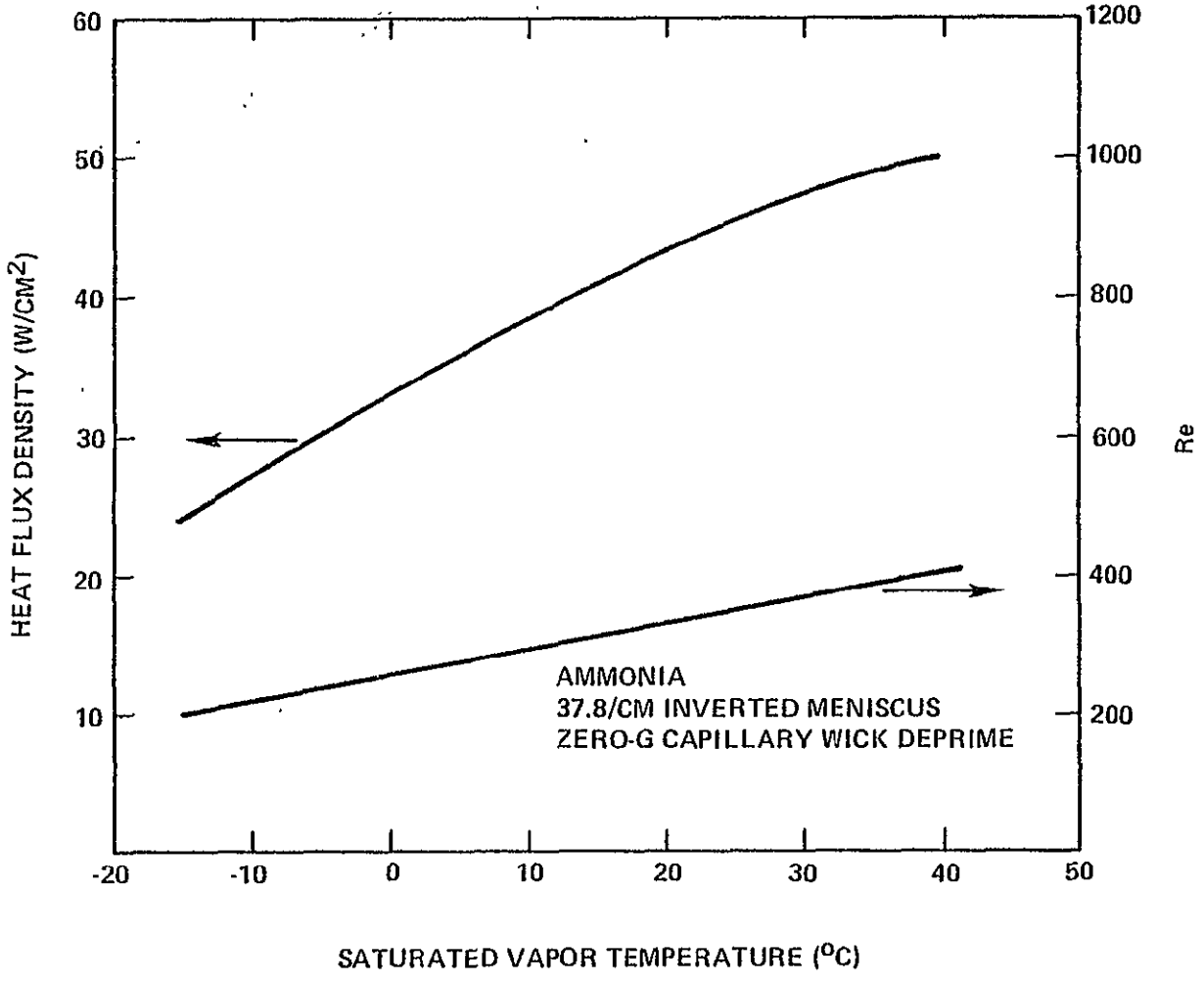

FIGURE 2.2-2. CALCULATED PEAK HEAT FLUX DENSITY AND CORRESPONDING AVERAGE VAPOR MICROCHANNEL REYNOLDS NUMBER FOR 37.8 CM^{-1} SURFACE

7705-124.8

TABLE 2-1. LAMINAR FRICTION FACTOR COEFFICIENT[1]
(F = c/Re)

Covered Groove Cross-Section	Coefficient "c"
tube (ref.)	16.0
rectangle (3.5:1)	17.75
square	14.25
equilateral triangle	13.25
isosceles right triangle	13.00

[1]From H. Schlicting, Boundary Layer Theory, McGraw-Hill, New York, 1968.

range -10^{o} to $-20^{o}C$, the maximum heat flux density is calculated to be 20 to 30 W/cm^2, while at $25^{o}C$, the maximum heat flux density is about 45 W/cm^2. This increase is primarily caused by a lower vapor phase pressure drop, which in turn is the result of an increased vapor density. The conclusion to be drawn is that quite high heat fluxes are possible before vapor core pressure drop is significant. Because of the large number of small parallel vapor channels, vapor flow Reynolds numbers on the order of 500 or less are typical for covered V-grooves with high-pressure fluids like ammonia.

For the case in which the liquid and vapor flow are co-current (Figure 2.2-1b), the maximum vapor-liquid pressure difference occurs generally at an intermediate point $0 < X < L/2$ because the highest vapor pressure is found at $X = 0$, while the lowest liquid pressure is found at $X = \pm L/2$. Therefore, the largest difference between these two pressures in general occurs at a position between $X = 0$ and $X = \pm L/2$.

If the liquid loss rate by evaporation from the capillary wick is assumed to be uniform over the area of contact with the wall, and if the rate of vapor injection into each microchannel is assumed independent of position, then the liquid and vapor pressures are, respectively,

$$P_\ell \simeq P_{vs} - \Delta P_{\ell o} - 4\Delta P_{\ell m}\left[\left|\frac{X}{L}\right| - \left(\frac{X}{L}\right)^2\right] \tag{2.2-6}$$

and

$$P_v \simeq P_{vs} + \Delta P_{vm}\left[1 - \left(\frac{2X}{L}\right)^2\right] \tag{2.2-7}$$

The largest difference between (2.2-6) and (2.2-7) occurs at

$$\left|\frac{X}{L/2}\right| = \frac{1}{1+\eta} \tag{2.2-8}$$

where

$$\eta = \Delta P_{vm}/\Delta P_{\ell m},$$

and the maximum pressure difference is

$$\Delta P_{\ell vm} = \Delta P_{\ell o} + \Delta P_{\ell m} \cdot \left(1 + \frac{\eta^2}{1+\eta^2}\right) \tag{2.2-9}$$

Examination of this equation shows that co-current flow reduces the maximum vapor-liquid pressure difference. For example, for the particular situation that $\eta = 1$ ($\Delta P_{vm} = \Delta P_{\ell m}$) and $\Delta P_{\ell o} = 0$, the maximum vapor-liquid pressure difference at the wall will be,

$$\Delta P_{\ell vm} = 2\,\Delta P_{\ell m} \qquad \text{(countercurrent flow, Fig. 2a)} \qquad (2.2\text{-}10)$$

$$\Delta P_{\ell vm} = 1.5\,\Delta P_{\ell m} \qquad \text{(cocurrent flow, Fig. 2b)} \qquad (2.2\text{-}11)$$

The peak heat flux density q_{am} would therefore be about 33% higher for cocurrent vapor-liquid flow.

Cocurrent flow may also be of benefit from a quite different standpoint. If liquid entrainment occurred in the vapor stream, this entrained liquid would be transported toward the groove end that was in most need of liquid, and nearest to a dry-out condition, whereas entrainment in countercurrent flow would accelerate dry-out. The subject of entrainment is discussed in more detail in the following section.

Entrainment

A second phenomenon that may occur with wick-covered grooves is liquid entrainment in the groove vapor stream or liquid wave formation because of liquid/vapor interfacial shear. These effects are both correlated by the Weber number,

$$We = \frac{\rho_v U_{av}^2 \lambda}{\sigma} \qquad (2.2\text{-}12)$$

where λ is the characteristic wavelength of the disturbance.

To a degree, entrainment and wave formation may be desirable because of potential improvement in heat transfer resulting from turbulent wave motion and from entrained droplet impingement on non-wetted groove surfaces. For a Weber number = 2π, large interfacial waves and entrainment are expected.[9] The characteristic wavelength λ for covered grooves will be on the order of the inscribed diameter $2 \cdot R$ (Figure 2.1-1). Weber numbers based on operating data are presented in Figure 2.2-3 for groove densities of 12.6 cm^{-1} and 37.8^{-1}

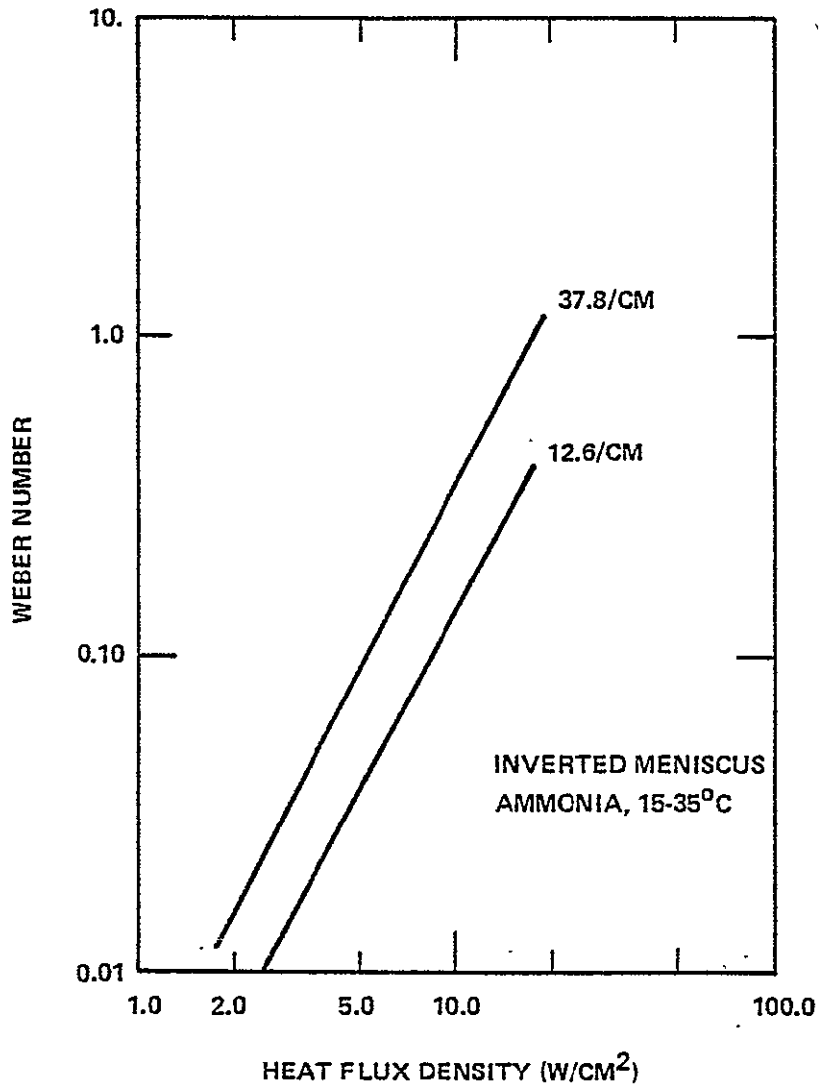

FIGURE 2.2-3. MICRO-CHANNEL WEBER NUMBER FOR ENTRAINMENT BASED ON INSCRIBED CIRCLE OF RADIUS "R"

7705-124.4

(with groove characteristic cross sections as in Figure 3-2), and it can be concluded that heat flux densities in excess of 50 W/cm^2 are required for the onset of entrainment or wave formation. In actual fact, the critical heat fluxes are even higher because the operating menisci are significantly smaller than $2 \cdot R$ at high power levels.

2.3 The Role of Thermal Constriction

Feldman and Berger[4] and Schneider et al.[16] have found that two-dimensional finite element conduction models of meniscus heat transfer indicate that most evaporative heat transfer from a grooved surface occurs over a relatively small zone near the fillet tip where the liquid film is quite thin. The heat transfer coefficient for a grooved surface is therefore dominated by heat transfer over a very small fraction of the total groove area. The overall thermal resistance of this small area can be considered the sum of a geometrical constriction resistance in the underlying metal plus a film conduction drop across the meniscus plus an interfacial resistance at the liquid-vapor interface. Of these three resistances, the liquid-vapor interfacial resistance is generally small, and will be neglected at this point. However, the relative importance of constriction and film conduction in defining evaporative heat transfer behavior is not as obvious, and a simple model of constriction heat transfer for rectangular grooves was generated.

In Figure 2.3-1, heat is removed at a uniform rate per unit area Q_a from an infinitely long bar over a strip of height "a". The heat is input to the bar over the bottom face, which is at a constant temperature. All other areas are insulated. The detailed calculations will not be presented, but the general solution technique was as follows. The heat conduction equation was solved for the bar using separation of variables and the following boundary conditions.

B.C.1 - at $x = 0$, $T = T_o$
B.C.2 - at $y = w$, $\partial T/\partial y = 0$
B.C.3 - at $x = b$, $\partial T/\partial x = 0$

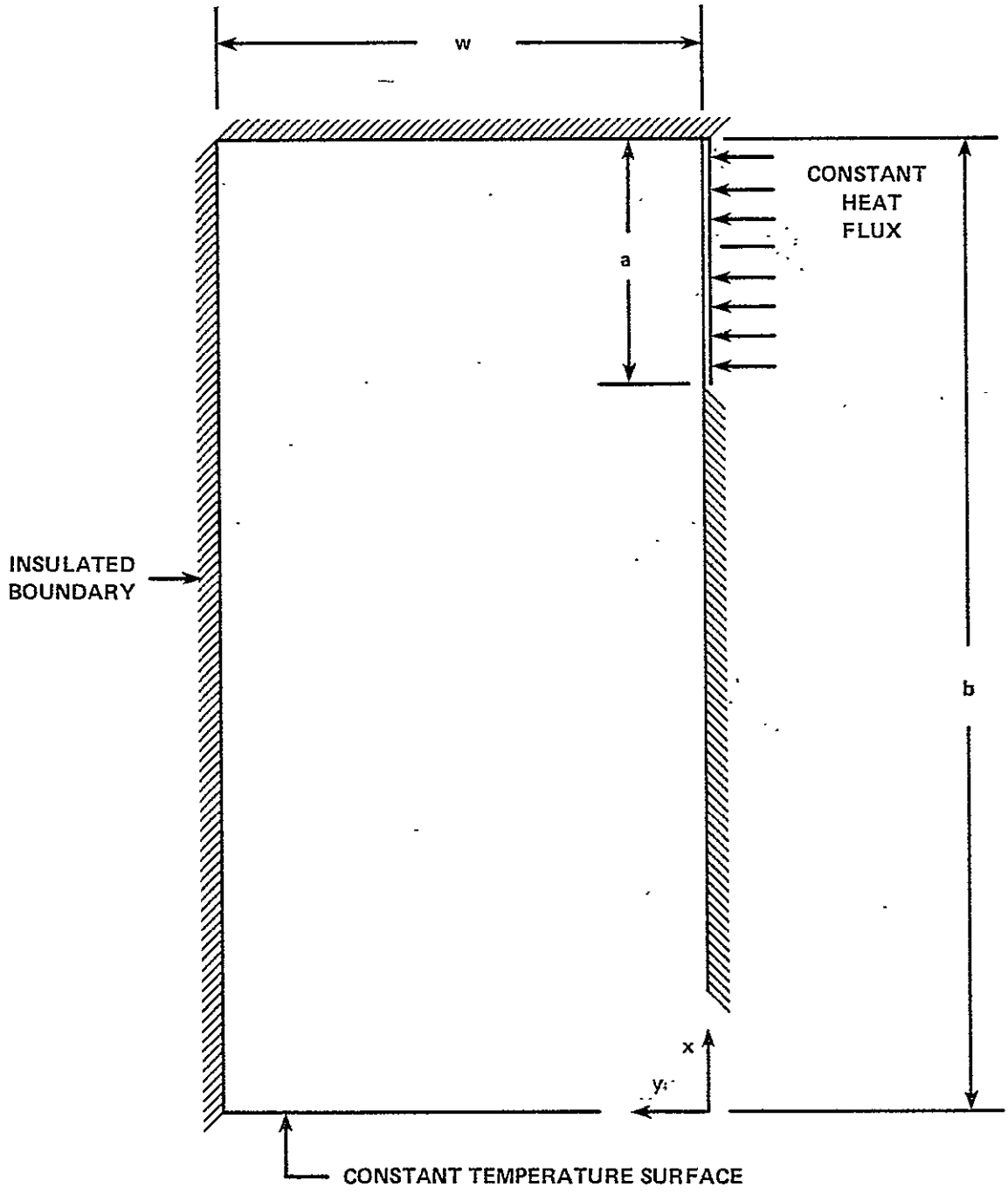

FIGURE 2.3-1. CONSTRICTION RESISTANCE IN AN INFINITELY LONG BAR OF HEIGHT b AND WIDTH w. ONE SIDE IS AT A CONSTANT TEMPERATURE, WHILE HEAT IS BEING APPLIED ON AN ADJACENT SIDE OVER A STRIP OF HEIGHT "a", AS SHOWN.

7705-124.15

B.C.4 - at $y = 0$, $0 \le x \le b-a$, $\partial T/\partial y = 0$

B.C.5 - at $y = 0$, $b-a \le x \le b$, $\partial T/\partial y = -Q_a/K_w$

where T_o is the base temperature and Q_a is a constant heat flux density. Once the temperature distribution was found, the average temperature over the spot $b-a \le x \le b$ was calculated. This immediately yielded the constriction resistance as

$$\frac{R_{th}K_w}{2} = \frac{1}{\pi^3}\left(\frac{b}{a}\right)^2 \sum_{K=1}^{\infty} \frac{\coth\left[\pi\,(K-\tfrac{1}{2})\,\frac{w}{b}\right]}{(K-\tfrac{1}{2})^3} \cdot \cos^2\left[\pi\,(K-\tfrac{1}{2})(1-\frac{a}{b})\right] \qquad (2.3\text{-}1)$$

$$R_{th} = \langle \Delta T \rangle / Q_\ell$$

where K_w is the bar thermal conductivity and Q_ℓ is the heat flux per unit length of bar (watts/cm).

The constriction factor $RK_w/2$ is presented in Figure 2.3-2 as a function of a/b for various ratios of w/b. The constriction resistance for a constant temperature spot boundary condition was found for a specific value of w/b using graphite resistance paper. A comparison of these resistance values with the constant heat flux model (equation 2.3-1) is given in Table 2.3-1. For small spot sizes, the constant temperature constriction resistance is about 6 % higher than the constant heat flux. However, it must be recognized that the accuracy of values derived from graphite resistance paper measurements is uncertain, and this percent difference cannot be totally ascribed to the differing boundary conditions.

For constriction resistance to be of significance in limiting film heat transfer, it must be shown to be comparable in value to the evaporative resistances demonstrated for various grooved heat pipes. A great deal of data exists for axial square-grooved and circumferential V-grooved heat pipes with groove densities on the order of 25/cm to 35/cm. For example, Schlitt, Kirkpatrick,

TABLE 2.3-1. A COMPARISON OF THEORETICAL CONSTRICTION RESISTANCE VALUES FOR THE INFINITE STRIP (FIGURE 2.3-1) WITH VALUES OBTAINED USING GRAPHITE RESISTANCE PAPER[1]

a/b	Thermal Resistance (Analog)	Thermal Resistance (Fourier series)	$\frac{R_A}{R_F}$
$4.31(10^{-4})$	7.65	7.09	1.08
$6.08(10^{-4})$	7.31	6.87	1.06
$1.18(10^{-3})$	6.97	6.446	1.08
$1.53(10^{-3})$	6.72	6.28	1.07
$7.31(10^{-3})$	5.50	5.29	1.04
$1.225(10^{-2})$	5.12	4.96	1.03
.0344	4.53	4.30	1.05
.0569	4.19	3.977	1.05
.0732	4.03	3.813	1.06
.122	3.635	3.473	1.05

[1] The analytical model incorporates a constant heat flux at one boundary, whereas resistance paper necessarily approximates constant temperature boundary conditions. w/b = 0.3235

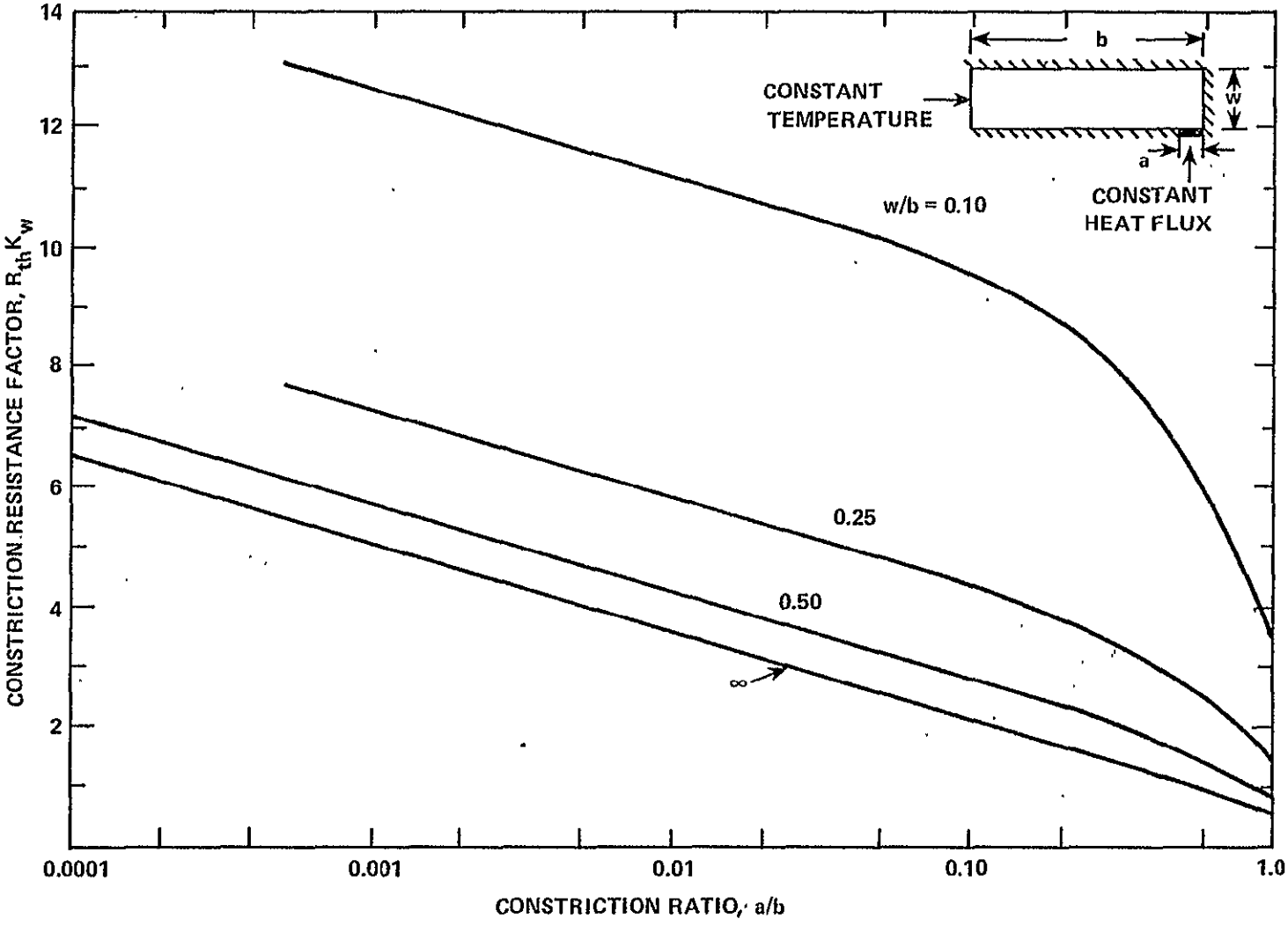

FIGURE 2.3-2. CONSTRICTION RESISTANCE FOR HEAT TRANSFER TO A RECTANGULAR BAR VIA A NARROW STRIP OF WIDTH "a"

7705-181.

and Brennan measured a heat transfer coefficient of 0.7 W/cm^2K with a 8.7 axial groove/cm aluminum heat pipe using ammonia at -23^oC.[10] If the heat transfer coefficient of Schlitt, et al. is considered to be the result of a series of parallel line heat transfer elements (that is, the meniscus tips), then the conductance per unit element length, or per unit fillet length, is

$$G_\ell = \frac{0.7}{2 \times 8.7} = 0.0402 \text{ W/cmK}$$

From Figure 2.3-2, the constriction resistance of a square groove (w/b = 0.50) is about 5.7 at $a/b = 10^{-3}$, and approximately 7.2 at $a/b = 10^{-4}$. Taking the most pessimistic case of $a/b = 10^{-4}$, this corresponds, for a 8.7/cm square groove, to a constriction width $a = 5.75 \times 10^{-6}$ cm, and a per-unit length fillet conductance of

$$G_\ell = \frac{K_w}{R_{th}} = \frac{2.36}{7.2} = 0.328 \text{ W/cmK} \qquad \text{(aluminum)}$$

This hypothetical contact zone of 575 Angstroms width has a lineal conductance that is a factor of 8.1 higher than the measured value. However, for stainless steel, which has a conductivity on the order of 0.15 W/cmK, the lineal conductance would be only 0.0208 W/cmK, and constriction resistance may be of some importance. For high conductivity metals, the wall-side conduction drop does not appear to be a dominant factor in defining the overall evaporative heat transfer coefficient.

2.4 One-dimensional Meniscus Heat Transfer Model

To gain a fundamental understanding of meniscus heat transfer, a one-dimensional evaporative heat transfer model has been developed that not only accounts for conduction in the fillet and underlying wall, but also considers fluid dynamics within the fillet. Two-dimensional models of fillet heat transfer generated by other investigators[4-6] have indicated that heat transfer primarily occurs over a very small region near the fillet tip. This means that a significant liquid flow must occur between each fillet base end tip, and that this flow must be pumped by surface tension forces. Since surface tension forces are intimately related to liquid-vapor interfacial curvature, it is quite possible that significant changes in surface curvature occur between the base and tip of each meniscus, leading to a flow-influenced film curvature and heat transfer coefficient.

For high thermal conductivity metals like aluminum, and for rectangular grooves, the constriction resistance analysis of Section 2.3 indicates that the conduction drop through the heat pipe wall and ground surface tooth is significantly smaller than the conduction drop across the liquid film, on the basis of comparisons with experimental evaporative heat transfer data. Therefore, a one-dimensional "fin equation" approach to heat transfer in the evaporator wall is considered adequate for engineering model purposes.

Fillet Hydrodynamics

If the liquid fillet is viewed as a hydrodynamic boundary layer, the governing Navier-Stokes equation is

$$U_x \frac{\partial U_x}{\partial x} + U_y \frac{\partial U_x}{\partial y} = \nu_\ell \frac{\partial^2 U_x}{\partial y^2} - \frac{1}{\rho_\ell} \frac{\partial P_\ell}{\partial x} \qquad (2.4\text{-}1)$$

where the coordinate system originates from the fillet tip and x- is parallel to the groove wall and y- is perpendicular to the wall (Figure 2.4-1). The liquid kinematic viscosity is ν_ℓ and the liquid density is ρ_ℓ. The liquid pressure P_ℓ is assumed independent of y.

In addition to the x-directed Navier-Stokes equation, conservation of mass gives

$$\frac{\partial U_x}{\partial x} + \frac{\partial U_y}{\partial y} = 0 \qquad (2.4\text{-}2)$$

The coupled system of equations (2.4-1) and (2.4-2) has as unknowns, U_x, U_y, and P_ℓ. To reduce this system to one more amenable to solution, the von Karman-Pohlhausen integral technique has been used. In essence, an educated guess is made of the form of the velocity distribution U_x. The boundary layer equation (2.4-1) and conservation equation (2.4-2) are integrated at constant x across the liquid film. The result is a more tractable coupled set of ordinary differential equations that satisfies (2.4-1) and (2.4-2) in an average sense. For the present problem the x-directed velocity is assumed to be parabolic in y,

$$U_x = A + By + Cy^2 \qquad (2.4\text{-}3)$$

At the wall, the x-directed fluid velocity is zero, while at the liquid-vapor interface the effects of shear are neglected ($\partial U_x/\partial y = 0$). The coefficients in equation (2.4-3), with these boundary conditions, yield the velocity profile

$$U_x = U_1 \left(2\left(\frac{y}{\delta}\right) - \left(\frac{y}{\delta}\right)^2\right) \qquad (2.4\text{-}4)$$

where δ is the local film thickness and U_1 is the x-directed liquid velocity at the liquid-vapor interface. The y-directed velocity can now be obtained from the continuity equation as

$$U_y = -\int_0^y \frac{\partial U_x}{\partial x}\, dy \qquad (2.4\text{-}5)$$

where use has been made of the boundary condition $U_y = 0$ at $y = 0$.

When the expressions (2.4-4) and (2.4-5) defining U_x and U_y, respectively, are substituted into the Navier-Stokes equation, and the equation is integrated over the range $0 \leq y \leq \delta$, the following equation in U_1 and δ results:

$$\frac{2}{5} U_1 \delta \frac{dU_1}{dx} - \frac{2}{15} U_1^2 \frac{d\delta}{dx} = \frac{-2\nu_\ell U_1}{\delta} - \frac{\delta}{\rho_\ell} \frac{dP_\ell}{dx} \tag{2.4-6}$$

To obtain a second equation, it is necessary to consider the relationship between film thickness and evaporation or condensation mass transfer. Specifically, for a small zone as shown in Figure 2.4-2, mass conservation requires that

$$\frac{Q_a}{h_{fg}} \cdot \Delta x = \rho_\ell \left(U_y \Big|_{y=\delta} \cdot \Delta x - U_1 \Delta\delta \right) \tag{2.4-7}$$

where Q_a is the local heat flux density and h_{fg} is the latent heat of vaporization per unit mass. The heat flux Q_a is positive for evaporation and negative for condensation. In the limiting case of small Δx and $\Delta\delta$, and using equation (2.4-5),

$$\frac{d}{dx} (\delta U_1) = - \frac{3}{2} \frac{Q_a}{\rho_\ell h_{fg}} \tag{2.4-8}$$

Equations (2.4-6) and (2.4-8) would now be solvable if Q_a and dP/dx were known.

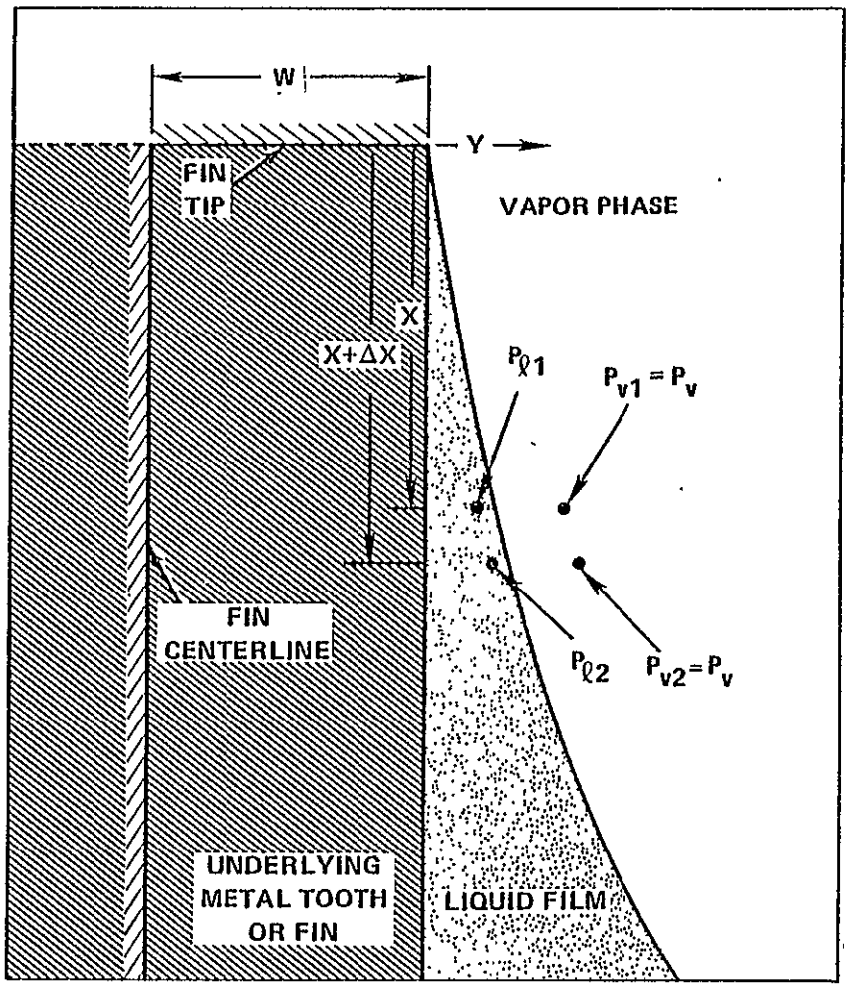

FIGURE 2.4-1. SCHEMATIC DRAWING OF MENISCUS HEAT TRANSFER MODEL SHOWING COORDINATE SYSTEM AND CHARACTERISTIC DIMENSIONS

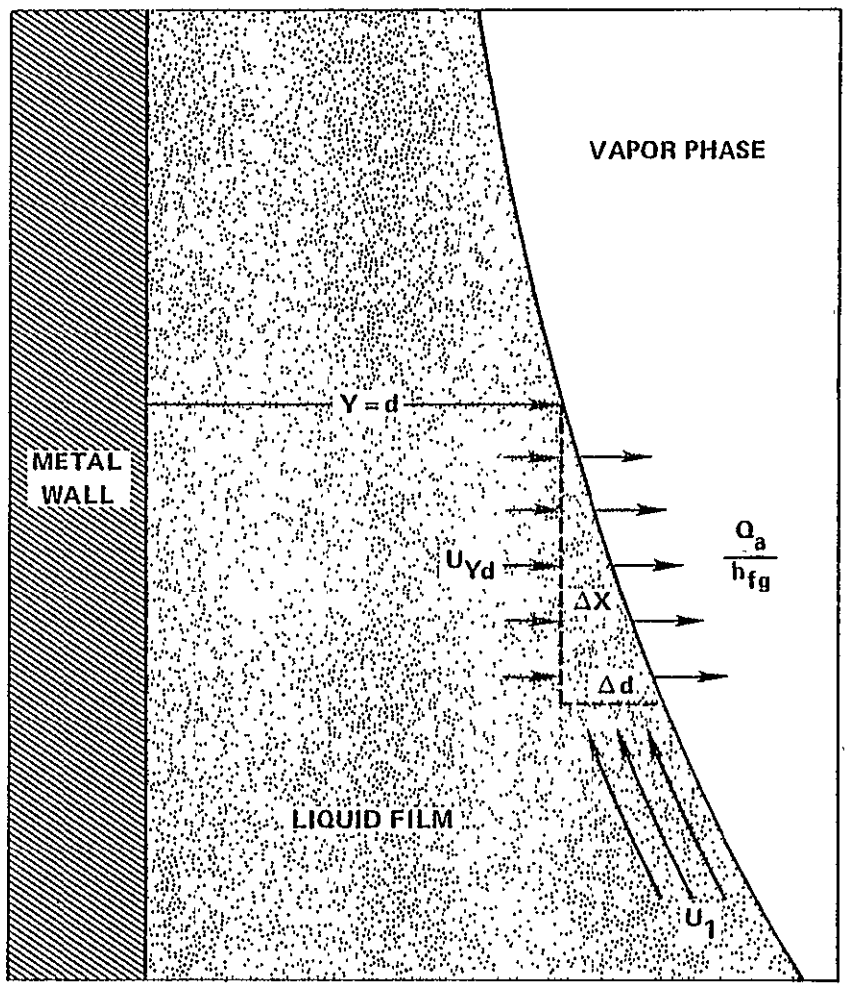

FIGURE 2.4-2. MASS BALANCE AT LIQUID-VAPOR INTERFACE. THE SYMBOL "d" IS EQUIVALENT TO THE SYMBOL "δ" IN THE TEXT.

7705-124.1

Heat Flux Model

The local heat flux is assumed to be determined by a film heat transfer coefficient (K_ℓ/δ) and a vaporization limit. The rate at which molecules undergo a phase change at the liquid-vapor interface is finite and governed by kinetic theory. Under the assumption that each molecule impacting on the surface is thermalized to the film temperature (accommodation coefficient = 1.0), the differential arrival rate is

$$\Delta\dot{m} = \sqrt{\frac{M}{2\pi R}} \left(\frac{P_\delta}{\sqrt{T_\delta}} - \frac{P_{vs}}{\sqrt{T_{vs}}} \right) \qquad (gm/cm^2\ sec) \qquad (2.4\text{-}9)$$

where M is the liquid molecular weight and P_δ and P_{vs} are respectively the film surface and vapor phase pressures. The corresponding film surface and vapor phase temperatures are T_δ and T_{vs}. The factor R is the gas constant.

If the working fluid saturation vapor pressure is given by an equation of the form

$$P_{vs} = \frac{P_o}{T^N} \cdot EXP\ (-\psi/T) \qquad (2.4\text{-}10)$$

where P_o, N and ψ are empirical curve-fit factors, and if the film vaporization temperature drop is small compared to the average system temperature T_m, then the interfacial heat transfer coefficient is given by

$$H_i = P_{vs} \left(\frac{M}{2\pi R T_m} \right)^{\frac{1}{2}} \left(\frac{h_{fg}}{T_m} \right) \left(\frac{\psi}{T_m} - (N + \tfrac{1}{2}) \right) \qquad (W/cm^2K) \qquad (2.4\text{-}11)$$

This vaporization heat transfer coefficient and the film coefficient form a series thermal network with an overall heat transfer coefficient $\overline{H}$ from wall to vapor phase.

$$\overline{H} = \frac{K_\ell}{\delta}\left(\frac{1}{1 + A_o/\delta}\right) \qquad (2.4\text{-}12)$$

where

$$A_o = \frac{K_\ell\, T_m^{5/2}}{44.33\, h_{fg}\, P_{vs}\, \sqrt{M} \cdot \left(\psi - (N+\tfrac{1}{2})\, T_m\right)} \quad (cm) \qquad (2.4\text{-}13)$$

and where P_{vs} is in atmospheres, h_{fg} is in Joules/g-mole, T_m is in K, and the liquid conductivity K_ℓ is in W/cm-K. The working fluid molecular weight is in gm/gm-mole. For ammonia at 20°C, the film vaporization process is thermally equivalent to the conduction drop across an ammonia film of 1.5×10^{-6} cm thickness.

The heat flux density Q_a is then given by

$$Q_a = \overline{H}\,(T_{vs} - T_w), \qquad (W/cm^2) \qquad (2.4\text{-}14)$$

where T_{vs} and T_w are the vapor phase and wall temperatures.

Pressure Gradient Model

For momentum transfer to be described by a unidirectional boundary layer approximation to the Navier-Stokes equations, the pressure gradient $\partial P/\partial y$ in the liquid film must be assumed everywhere to be negligibly small. The only significant pressure change occurs in the direction of flow; that is, in the x-direction. If the fillet has only a one-dimensional curvature, and the vapor phase above the fillet is assumed to be at constant pressure, then changes in liquid pressure within the fillet must correspond exactly to changes in surface curvature: that is, the changing surface curvature is actually the mechanism by which liquid is fed to the meniscus tip. This situation is shown in Figure 2.4-1. The liquid pressure at any film cross-section is virtually constant, and hence the pressure difference at vertical position "x" between the point "ℓ1" in the liquid and point "v1" in the vapor is

$$P_{\ell 1} - P_{v1} = \frac{-\sigma}{r_1} \qquad (2.4\text{-}15a)$$

where r_1 is the local one-dimensional liquid surface curvature and σ is the liquid surface tension. At a position slightly further down the film, "x + Δx", the corresponding pressure balance is

$$P_{\ell 2} - P_{v2} = \frac{-\sigma}{r_2} \qquad (2.4\text{-}15b)$$

Since the vapor pressure is assumed constant ($P_{v1} = P_{v2}$), in the limit of Δx becoming vanishingly small the liquid pressure P_ℓ depends on the curvature "r" in the following way.

$$\frac{d}{dx}(P_\ell) = -\frac{d}{dx}\left(\frac{1}{r}\right) \qquad (2.4\text{-}15c)$$

Using the cartesian coordinate expression for surface curvature, the liquid pressure drop is

$$\frac{dP_\ell}{dx} = -\sigma \frac{d}{dx}\left(\frac{d^2\delta/dx^2}{\left(1 + \left(\frac{d\delta}{dx}\right)^2\right)^{3/2}}\right) \qquad (2.4\text{-}15d)$$

Conduction Drop in Metal Tooth or Fin

For modeling of heat transfer through the underlying metal tooth or fin, the classic one-dimensional fin equation has been used. The metal tooth of Figure 2 is assumed to be a fin of width 2w, and the local fin temperature T_w is given by

$$\frac{d^2T_w}{dx^2} = \frac{\bar{H}}{wk_w}(T_w - T_{vs}) \qquad (2.4\text{-}16)$$

where k_w is the metal conductivity, and $\bar{H}$ is given by Equation 2.4-12.

Model Summary

By incorporating the expressions for Q_a, dP_ℓ/dx, and T_w developed above, the final coupled differential equations in film thickness δ, the film surface velocity U_1, and wall temperature T_w are

$$\frac{d^3\delta}{dx^3} = \frac{3}{\gamma} \cdot \frac{d\delta/dx}{\left(1+\left(\frac{d\delta}{dx}\right)^2\right)}\left(\frac{d^2\delta}{dx^2}\right)^2 + \frac{\left(1+\left(\frac{d\delta}{dx}\right)^2\right)^{3/2}}{\gamma}\left[\frac{2uU_1}{\delta^2} - \frac{3}{5}\frac{Q_a}{h_{fg}} \cdot \frac{U_1}{\delta} - \frac{8}{15}\frac{\rho_\ell U_1^2}{\delta} \cdot \frac{d\delta}{dx}\right] \tag{2.4-17}$$

$$\frac{dU_1}{dx} = -\frac{3}{2}\frac{Q_a}{\rho_\ell h_{fg}}\left(\frac{1}{\delta}\right) - \frac{U_1}{\delta} \cdot \frac{d\delta}{dx} \tag{2.4-18}$$

and

$$\frac{d^2T_w}{dx^2} = \frac{\bar{H}}{wk_w}\left(T_w - T_{vs}\right) \tag{2.4-19}$$

The resulting equations are third-order, first-order, and second order. The equations were solved using a coupled 4th order Runge-Kutta integration method. If the equations are posed as follows,

$$y''' = f(y, y', y'', U, T) \qquad (T \equiv T_w) \tag{2.4-20}$$

$$U' = g(U, y, y', T) \tag{2.4-21}$$

$$T'' = h(T, y) \tag{2.4-22}$$

then the integration formulas are as follows, where "i+1" denotes the Runge-Kutta predicted value at the next step and "i" represents the present value of the variable.

$$U_{i+1} = U_i + \frac{\Delta x}{6}(w_1 + 2w_2 + 2w_3 + w_4) \quad (2.4\text{-}23)$$

$$y''_{i+1} = y''_i + \frac{\Delta x}{6}(k_1 + 2k_2 + 2k_3 + k_4) \quad (2.4\text{-}24)$$

$$y'_{i+1} = y'_i + \frac{\Delta x^2}{6}(k_1 + k_2 + k_3) + \Delta x y''_i \quad (2.4\text{-}25)$$

$$y_{i+1} = y_i + \frac{\Delta x^3}{12}(k_1 + k_2) + \Delta x y'_i + \frac{\Delta x^2}{2} y''_i \quad (2.4\text{-}26)$$

$$T'_{i+1} = T'_i + \frac{\Delta x}{6}(N_1 + 2N_2 + 2N_3 + N_4) \quad (2.4\text{-}27)$$

$$T_{i+1} = T_i + \frac{\Delta x^2}{6}(N_1 + N_2 + N_3) + \Delta x T'_i \quad (2.4\text{-}28)$$

To obtain the first values K_1, W_1, and N_1, the equations 20 through 22 are evaluated at the immediate position "i"; that is

$$K_1 = f(y_i, y'_i, y''_i, U_i, T_i) \quad (2.4\text{-}29)$$

$$W_1 = g(U_i, y_i, y'_i, T_i) \quad (2.4\text{-}30)$$

$$N_i = h(T_i, y_i) \quad (2.4\text{-}31)$$

To obtain the values K_2, W_2, and N_2, the equations 20 through 22 are evaluated with the following variable values.

$$y = y_i + \frac{\Delta x}{2} y'_i \quad (2.4\text{-}32)$$

$$y' = y'_i + \frac{\Delta x}{2} y''_i \quad (2.4\text{-}33)$$

$$y'' = y''_i + \frac{\Delta x}{2} K_1 \quad (2.4\text{-}34)$$

$$U = U_i + \frac{\Delta x}{2} W_1 \quad (2.4\text{-}35)$$

$$T = T_i + \frac{\Delta x}{2} T'_i \quad (2.4\text{-}36)$$

To obtain the values K_3, W_3, and N_3, the equations 2.4-20 through 2.4-22 are evaluated with the following variable values.

$$y = y_i + \frac{\Delta x}{2} y_i' + \frac{\Delta x^2}{4} y_i'' \quad (2.4\text{-}37)$$

$$y' = y_i' + \frac{\Delta x}{2} y_i'' + \frac{\Delta x^2}{4} K_1 \quad (2.4\text{-}38)$$

$$y'' = y_i'' + \frac{\Delta x}{2} K_2 \quad (2.4\text{-}39)$$

$$U = U_i + \frac{\Delta x}{2} W_2 \quad (2.4\text{-}40)$$

$$T = T_i + \frac{\Delta x}{2} T_i' + \frac{\Delta x^2}{4} N_1 \quad (2.4\text{-}41)$$

To obtain the values K_4, W_4, and N_4, the equations 2.4-20 through 2.4-22 are evaluated with the following variable values.

$$y = y_i + \Delta x y_i' + \frac{\Delta x^2}{2} + \frac{\Delta x^3}{4} K_1 \quad (2.4\text{-}42)$$

$$y' = y_i' + \Delta x y_i'' + \frac{\Delta x^2}{2} K_2 \quad (2.4\text{-}43)$$

$$y'' = y_i'' + \Delta x K_3 \quad (2.4\text{-}44)$$

$$U = U_i + \Delta x W_3 \quad (2.4\text{-}45)$$

$$T = T_i + \Delta x T_i' + \frac{\Delta x^2}{2} N_2 \quad (2.4\text{-}46)$$

Although the problem statement appears formidable and the third-order differential equation has a variety of non-linear terms, the solutions were found to be quite well-behaved.

Starting the Solution

Runge-Kutta integration is basically a shooting technique, and for a coupled third order differential equation system, initial values must be assigned for δ, $d\delta/dx$, $d^2\delta/dx^2$, U_1, T, and dT/dx. For reasons of computing economy, it is preferable to begin the solution at the fillet tip, $x = 0$. At $x = 0$, the intuitive substitution $\delta = 0$ is not satisfactory since several terms in the differential equations are divided by δ. Instead, δ must be set to a value less than the equivalent film evaporation thickness, which in the case of ammonia is about 1.5×10^{-6} cm at 20^{o}C. This initial value does not then dominate heat flow at the meniscus tip, and a local "sonic limit" is therefore assumed. The initial value of $d\delta/dx$ is the tangent of the contact angle. A contact angle of 1^{o} has been assumed for initial calculations. The second derivative $d^2\delta/dx^2$ is undetermined and can be arbitrarily set. However, it has been found that physically realistic meniscus conditions dictate a rather narrow range of appropriate second derivatives. If, for example, the initial value of $d^2\delta/dx^2$ is too small, the film will not grow properly away from the meniscus tip, and in some cases the film will actually thin down and vanish, much like the simulation of an evaporating droplet on a hot surface. The value of T (the wall temperature) at the tip is also undetermined, but the insulated behavior for $x = 0$ requires $dT/dx = 0$ at $x = 0$. At the boundary $x = 0$, the x-directed film surface velocity has been set to zero. In summary, typical starting conditions for ammonia modeling are:

1. $x = 0$
2. $\delta = 1\ (10^{-7})$ cm
3. $d\delta/dx = 0.01746$
4. $d^2\delta/dx^2$ = variable
5. $U_1 = 0$
6. T = variable
7. $dT/dx = 0$

The extremely low equivalent film conduction drop for evaporating ammonia (1.5×10^{-6} cm equivalent film thickness) poses a physical interpretation problem. For an actual film thickness much less than this value (1.0×10^{-7}

cm, for example), the molecular structure of the fluid may render this continuum analysis invalid. At a film thickness of 1.0×10^{-7} cm, the film is only a few molecules thick.

This problem also shows up in calculated meniscus profiles as a need for an extremely high starting value for $d^2\delta/dx^2$. The heat flux density is so high in this region that the predicted curvature pressure is on the order of an atmosphere below the general vapor core pressure. This means, among other things, that there could actually be a film boiling process at the meniscus tip, not attributable in total to wall superheat, but also to a very low liquid phase pressure.

Sample Solution

Figures 2.4-3a and 2.4-3b present results computed for an ammonia meniscus in contact with a rectangular aluminum tooth of 0.020 cm (the width "w" is therefore 0.010 cm). In Figure 2.4-3a, the film thickness and percent of total heat transfer are shown as a function of distance from the meniscus tip. Total meniscus depth is about 0.0105 cm, measured from the meniscus tip to the meniscus centerline position, while about 50% of the total heat is transferred in the first 10% of this distance, confirming the importance of this thin-film region.

In Figure 2.4-3b, the film thickness calculated with the present analysis is compared with the film thickness that would be expected if the meniscus were cylindrical in shape, as has been generally assumed for conduction modeling of meniscus heat transfer. For distances less than 0.5 (10^{-3}) cm, this comparison has not been done in Figure 2.4-3b because of the non-zero contact angle. However, for distances greater than 0.5 (10^{-3}) cm, where contact angle effects are negligible, the predicted film thickness is from 1.5 to 5 times greater than the cylindrical meniscus approximation. This is caused by a liquid phase pressure drop parallel to the underlying wall that is

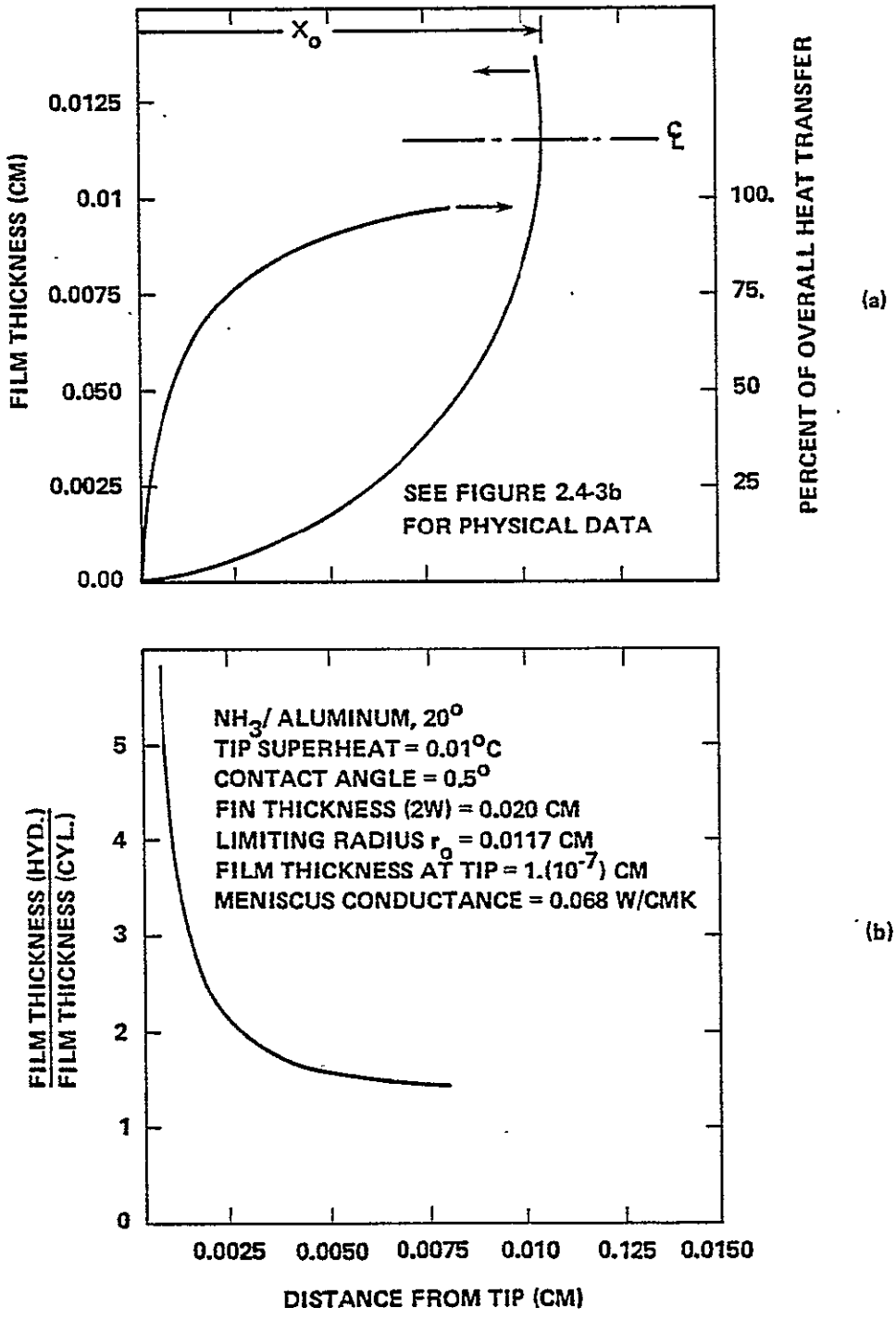

FIGURE 2.4-3 a, b. TYPICAL COMPUTATIONAL RESULTS FOR A SINGLE MENISCUS CONTACTING A METAL TOOTH OF 0.020 CM TOTAL WIDTH. IN FIGURE 2.4-3b, THE COMPUTED FILM THICKNESS IS COMPARED WITH THE THICKNESS EXPECTED FOR A CYLINDRICAL MENISCUS OF RADIUS r_o. BECAUSE OF LIQUID FILM HYDRODYNAMICS, THE FILM THICKNESS DEVIATES CONSIDERABLY FROM THAT CHARACTERISTIC OF A CYLINDRICAL INTERFACE.

7705-181.2

associated with liquid transport to the meniscus tip. This analysis indicates, at least for the limiting case of meniscus recession to the wetting angle, that fillet hydrodynamics is a crucial parameter in evaporation from grooved surfaces.

If a meniscus conductance is defined on the basis of the temperature difference between the wall at $x=x_o$ and the saturated vapor, then the lineal fillet conductance is 0.068 W/cmK. If it is assumed that the actual physical system corresponds to a 0.020 cm square groove, then the conductance based on the groove root temperature is 0.066 W/cmK. For a 0.01^{o}C superheat at the fillet tip, the lineal heat flux is about 0.0173 watt/cm, which translates into 0.865 watt/cm^2 for a uniform groove density of 25/cm, and a heat transfer coefficient of 3.3 W/cm^{2}K.

Conventional V-grooved ammonia/aluminum heat pipes with 25 grooves/cm have typically shown heat transfer coefficients on the order of 0.5 to 0.8 W/cm^{2}K, while data presented in a later section for the inverted meniscus show a heat transfer coefficient of about comparable magnitude for a 37.8/cm grooved surface at 0.865 W/cm^2. Therefore, the heat transfer coefficient predicted by the present model is about a factor of 5 higher than actual measured values. Additional analysis is required to determine the basis for this rather large difference. On a speculative level, this difference may be attributable to larger contact angles, nucleate boiling within the meniscus, or to a two-dimensional constriction resistance in the underlying wall, although the latter is not considered highly probable, as discussed in Section 2.3.

In other calculations for groove densities on the order of 10/cm, fillet conductances of about 0.075 W/cmK were calculated, while the axial U-groove data of Schlitt et al.[10] for 8.7 grooves/cm, as discussed in Section 2.3, yield a fillet conductance of 0.0402 W/cmK. Experimental fillet conductances, therefore, appear to be in better agreement with calculations for U-groove surfaces with low linear groove densities.

3.0 EXPERIMENTAL EQUIPMENT

To test the performance of the inverted meniscus concept with various groove densities, a heat pipe was constructed with a short cylindrical evaporator section as detailed in Figure 3.1. The active evaporator surface is 3.81 cm long and 1.27 cm in diameter for a total internal surface area of 15.20 cm^2. The aluminum evaporator assemblies were fabricated with circumferential groove densities of 12.6 cm^{-1}, 25 cm^{-1}, and 37.8 cm^{-1}, as in Figure 3.2. The grooves in each evaporator were cut as a single continuous spiral groove with a nominal 65^o included angle. After the grooving process, a finishing cut was taken along the axis of the evaporator to produce the characteristic flat-topped groove shape shown in Figure 3.2. This final cut produces a uniform internal tube diameter and minimizes the possibility of groove tip deformation during installation of the liquid transport wick. The 25 cm^{-1} evaporator was constructed for an earlier study,[8] and different machining techniques resulted in a groove profile resembling a half-cylinder rather than a V-groove.

The evaporator heater in each case consisted of a single layer of spiral-wrapped Inconel ribbon. The ribbon material was 0.16 cm wide, and was wrapped on a single layer of 0.009-cm-thick Teflon tape. The gap between each spiral wrap of ribbon was 0.11 cm, and was used as a pass-through zone for evaporator thermocouples. A layer of DC 340 applied to the heater winding assisted in maintaining uniform and adequate thermal contact of the ribbon with the Teflon film. The ribbon heater assembly and thermocouple leads were potted in a flexible silicone blanket such that the blanket has an outside diameter identical to the outside diameter of the evaporator end flanges. The silicone material stabilized the relative position of the heater ribbon and thermocouple leads so that the possibility for direct contact of the heater ribbon with the thermocouple leads was minimized.

The evaporators were each thermally monitored with 12 thermocouples inserted radially to a depth of 0.46 cm in the 0.62 cm thick evaporator wall. Eight of the thermocouples were inserted at 90^o intervals in proximity to the two end flanges, while the remaining four thermocouples were spaced at 90^o intervals in the center of the evaporator.

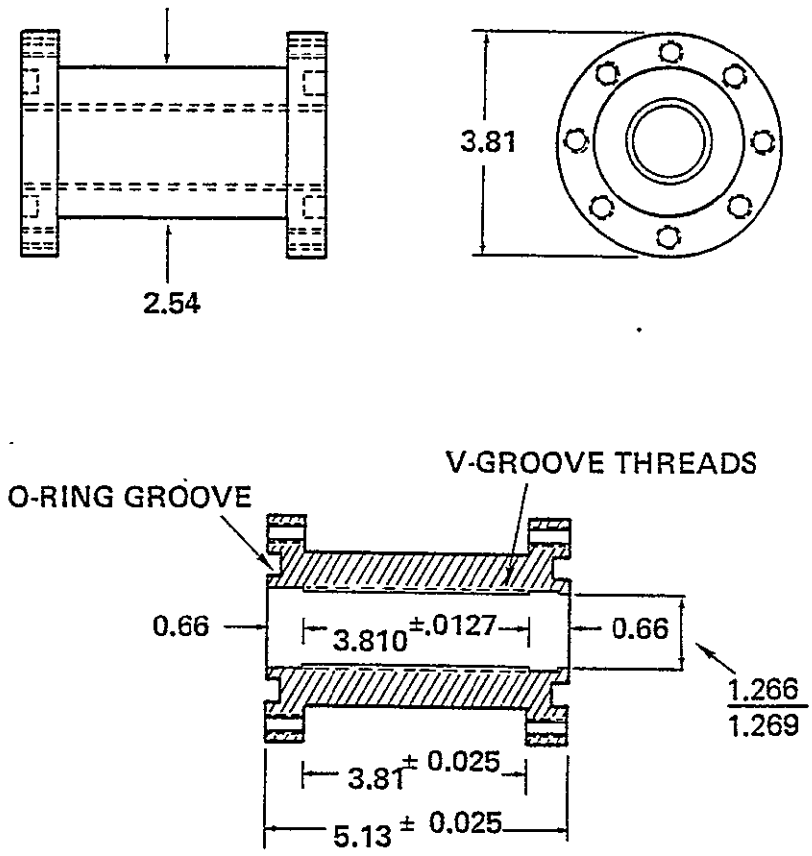

FIGURE 3-1. EVAPORATOR ASSEMBLY FOR INVERTED MENISCUS TESTING IN CYLINDRICAL GEOMETRY. ALL DIMENSIONS IN CENTIMETERS.

7705-124.7

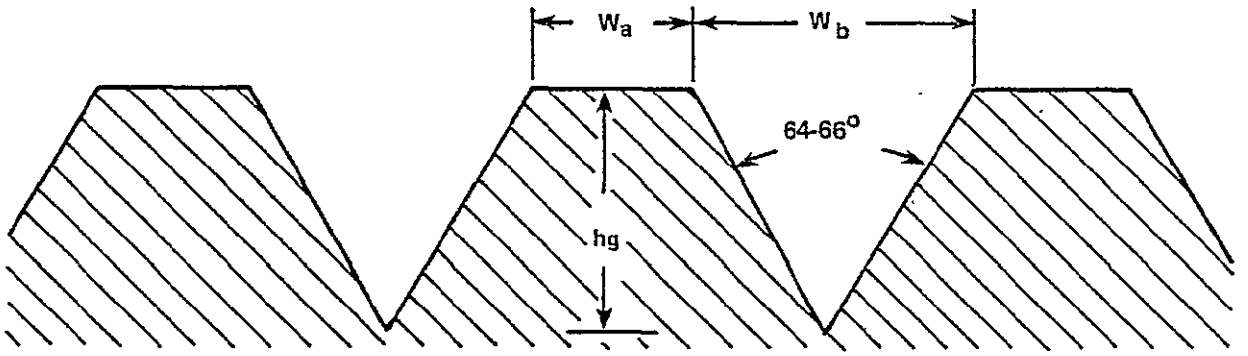

12.6 GROOVES/CM

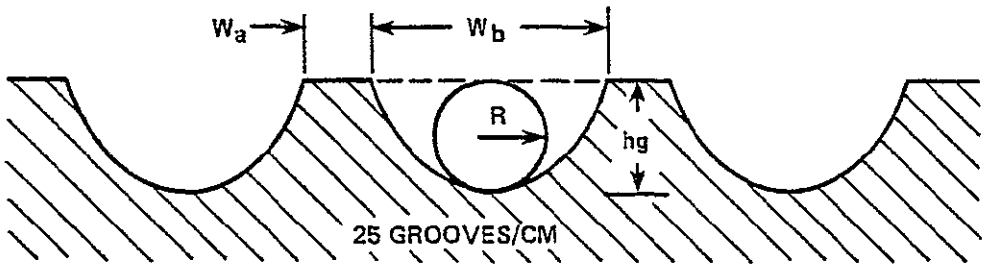

25 GROOVES/CM

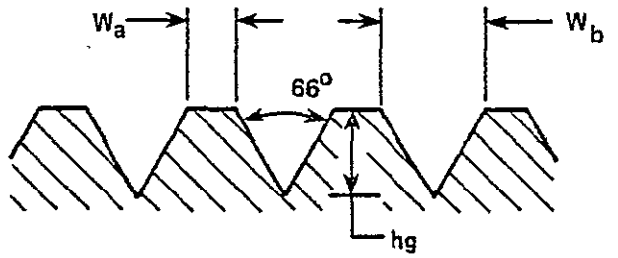

37.8 GROOVES/CM

CHARACTERISTIC DIMENSION (CM)	VALUES GROOVE DENSITY (GROOVES/CM)		
	12.6	25.0	37.8
W_a	0.0260	0.0081	0.0069
W_b	0.0534	0.0319	0.0196
hg	0.0421	0.0161	0.0151
R	0.0146	0.0078	0.0053

FIGURE 3-2. CROSS-SECTIONAL VIEWS OF SPIRAL GROOVE EVAPORATING SURFACES

7705-124.10

An adiabatic section 45 cm in length was used for all tests, while a condenser length of 15 cm was used for the 25 cm^{-1} tests, and a 30 cm length for the tests performed with 12.6 and 37.8 cm^{-1} grooved evaporators. A blind-end, thin-walled stainless steel tube 0.32 cm in diameter and 30 cm in length was inserted from the far end of the condenser to monitor vapor core temperature.

A close-fitting guide tube covered with seven layers of 400 mesh stainless steel screen served as a wick to distribute liquid circumferentially to the screw threads for the 12.6 cm^{-1} tests, while six layers were used in the 25 cm^{-1} tests. A cross-sectional detail of this wicking structure is presented in Figure 3.3. The guide tube incorporated two 0.108-cm-wide axial slots so that the screens may be drawn tightly over the tube and inserted through the slots to be spot-welded to the inner surface of the guide tube, and to provide a means for vapor escape from the grooves. The slots together account for 5.4% of the interface area. The layers of screen are allowed to overlap on the inside guide tube diameter to provide an area for the axial wick to transfer fluid to the circumferential wick. As assembled, the screen-covered tube is perhaps 0.0025 cm larger than the I.D. of the grooved evaporator, but inherent looseness in a multilayer wick allows the guide tube and wick to be inserted.

To ensure adequate fluid transport to the evaporator section, the axial wick shown in Figure 3.4 was used. This multiple-tube artery consisted of 19 screened single-layer tubes of 0.076 cm O.D. fitted into an outer wrap of 0.457 cm diameter. All screens used were 400 mesh square-weave stainless steel. The liquid was transported from the axial wick to the circumferential wick by four multiple-layer screen tubes. In the 25 cm^{-1} tests, the tubes consisted of 6 layers of screen, while later tests with 12.6 and 37.8 cm^{-1} surfaces used 8 layers of screen. Except for very low power operation, the central holes in these screened tubes remained unprimed. A summary of heat pipe mechanical design and zero-g transport capacities are given in Table 3.1. Axial flow conductance of the artery was calculated using the hydraulic

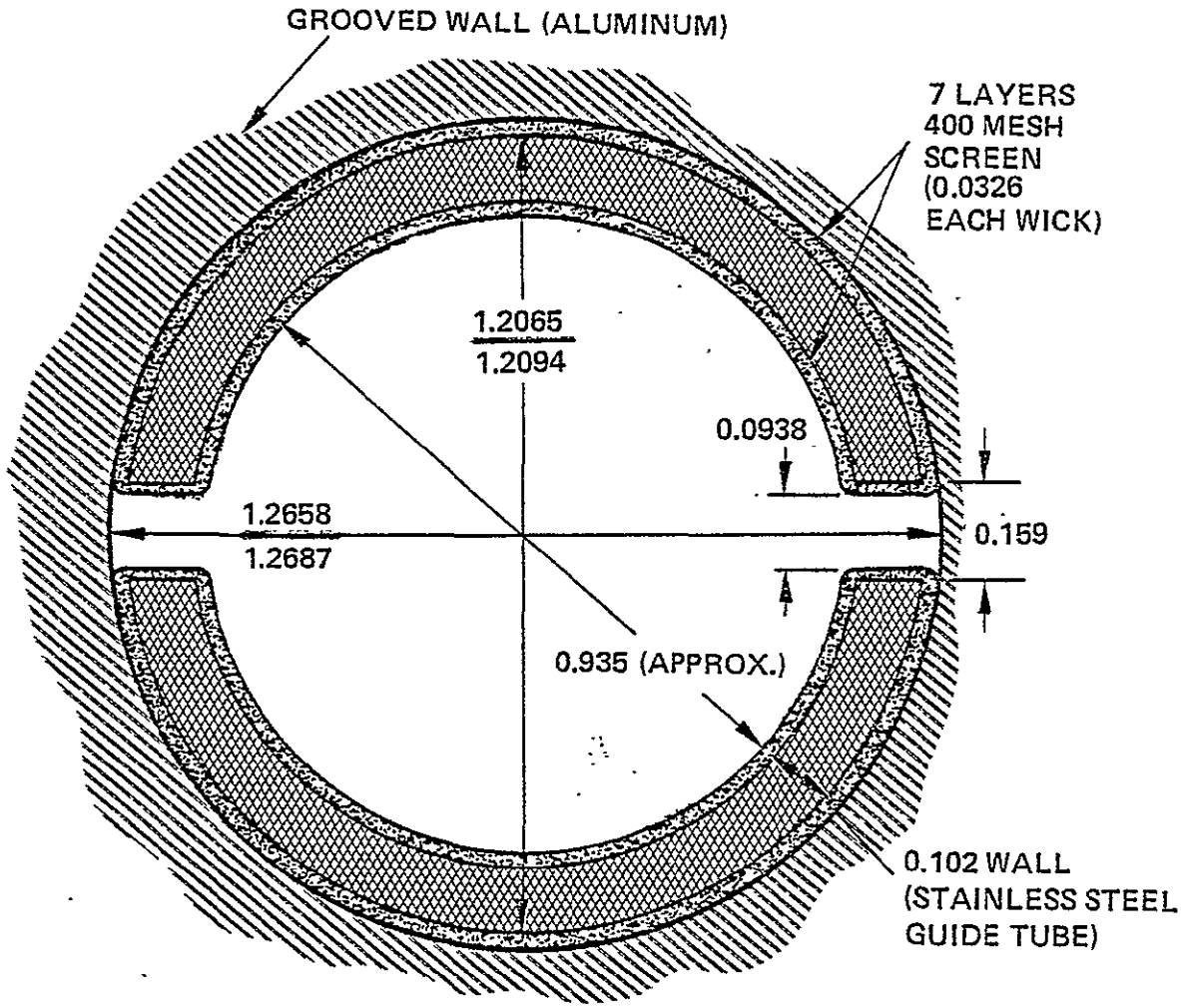

FIGURE 3-3. SECTIONAL VIEW OF INVERTED MENISCUS HEAT PIPE EVAPORATOR SHOWING DETAILS OF CIRCUMFERENTIAL EVAPORATIVE TRANSPORT WICK. NOTE STAINLESS STEEL GUIDE TUBE FOR ACCURATELY PLACING CIRCUMFERENTIAL WICK IN CONTACT WITH GROOVED WALL. TOTAL HEAT TRANSFER AREA IS 15.2 CM^2. ALL DIMENSIONS IN CM.

7705-124.5

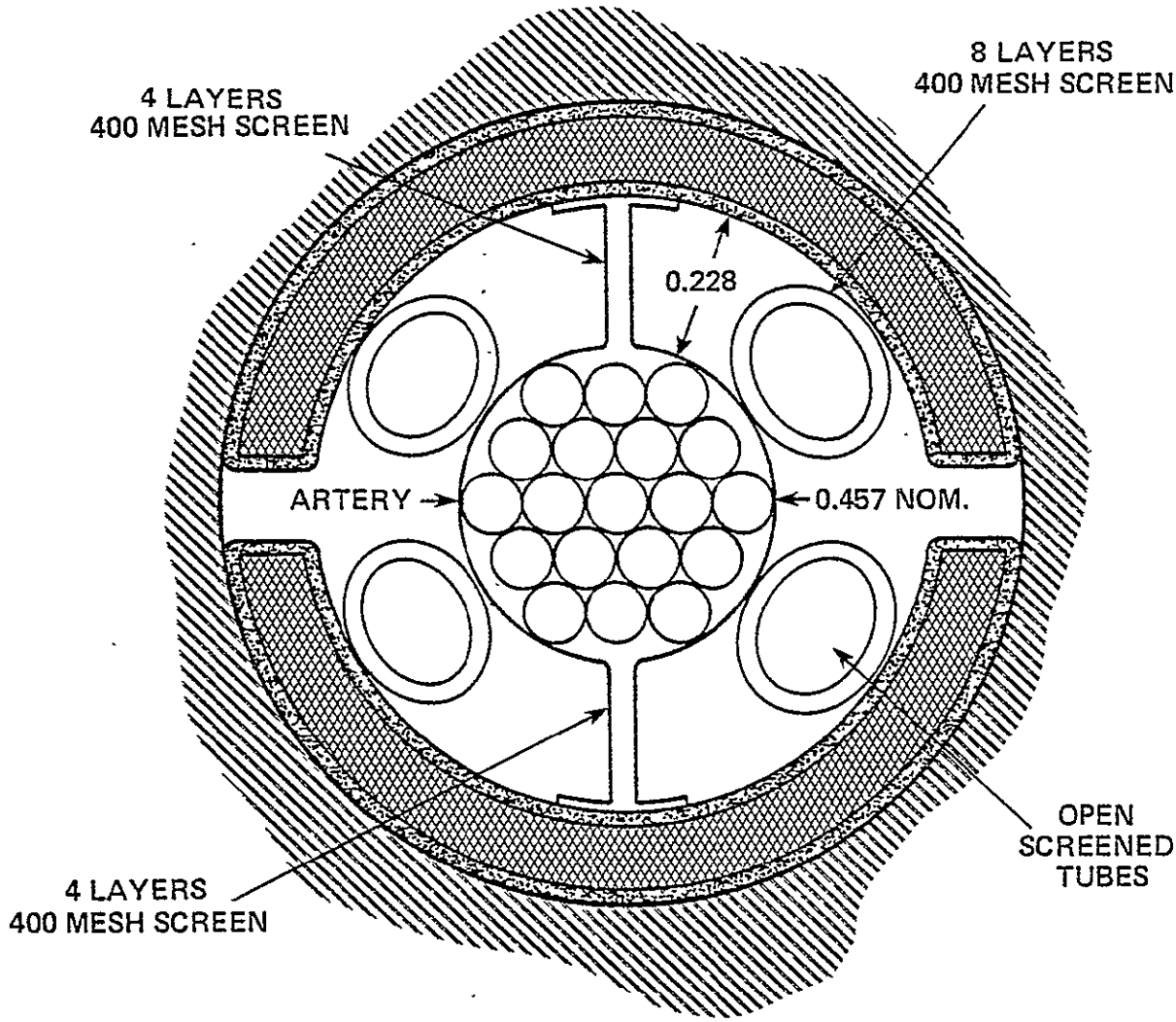

FIGURE 3-4. SECTIONAL VIEW OF INVERTED MENISCUS HEAT PIPE EVAPORATOR WITH MULTIPLE-TUBE ARTERY AND SCREENED TUBE RADIAL TRANSPORT WICKS. ALL DIMENSIONS IN CM.

7705-124.6

TABLE 3.1. HEAT PIPE SPECIFICATIONS

Parameter	12.6 and 37.8 cm^{-1} Tests	25 cm^{-1} Tests
Evaporator I.D.(1), cm	1.27	1.27
Evaporator length, cm	3.81	3.81
Adiabatic length, cm	45.1	45.1
Condenser length, cm	30.5	15.2
Axial transport wick	19 tube bundled artery, 400 mesh square weave screen	
Max. capillary pumping pressure (exptl.), dynes/cm^2	12,600 at = 20.1 dynes/cm	
Calculated transport capacity, watts @ 25°C(2)	772/407	545

(1) To inner faces of threaded section

(2) Includes vapor flow pressure drop

diameter method discussed in Reference 11, while liquid and vapor pressure drops in the evaporator were calculated following the procedures discussed in Section 2.1. Capacity predictions corrected for 1 g but not for a liquid pool, are shown in Figure 3.5, along with various test points. Test point adverse tilts are corrected for liquid puddling, but the overfill used to ensure priming of the multiple tube artery will influence in an undetermined fashion experimental capacities at low adverse tilts. As discussed at a later point, the effect of this pool on effective heat pipe length and adverse tilt were empirically determined in auxiliary tests. Heat transfer data was taken at adequate tilt to ensure recession of the liquid into the condenser.

Experimental Technique

Once the component parts of the heat pipe were cleaned and assembled, the heat pipe was flushed with several anhydrous ammonia charges and evacuated. The final charge used for data acquisition was approximately a 40% overcharge relative to the arterial structure. This overfill was used to ensure priming of the axial artery. The influence of the pool resulting from overcharge on heat pipe effective length and adverse tilt was empirically determined in a glass tube of identical inside diameter as the heat pipe using the multitube artery and isopropyl alcohol to simulate ammonia priming behavior. After charging, the heat pipe was allowed to remain stagnant for 1-2 hours in a horizontal position to aid in the venting of gas occlusions. At this point, the heat pipe was considered primed and charged.

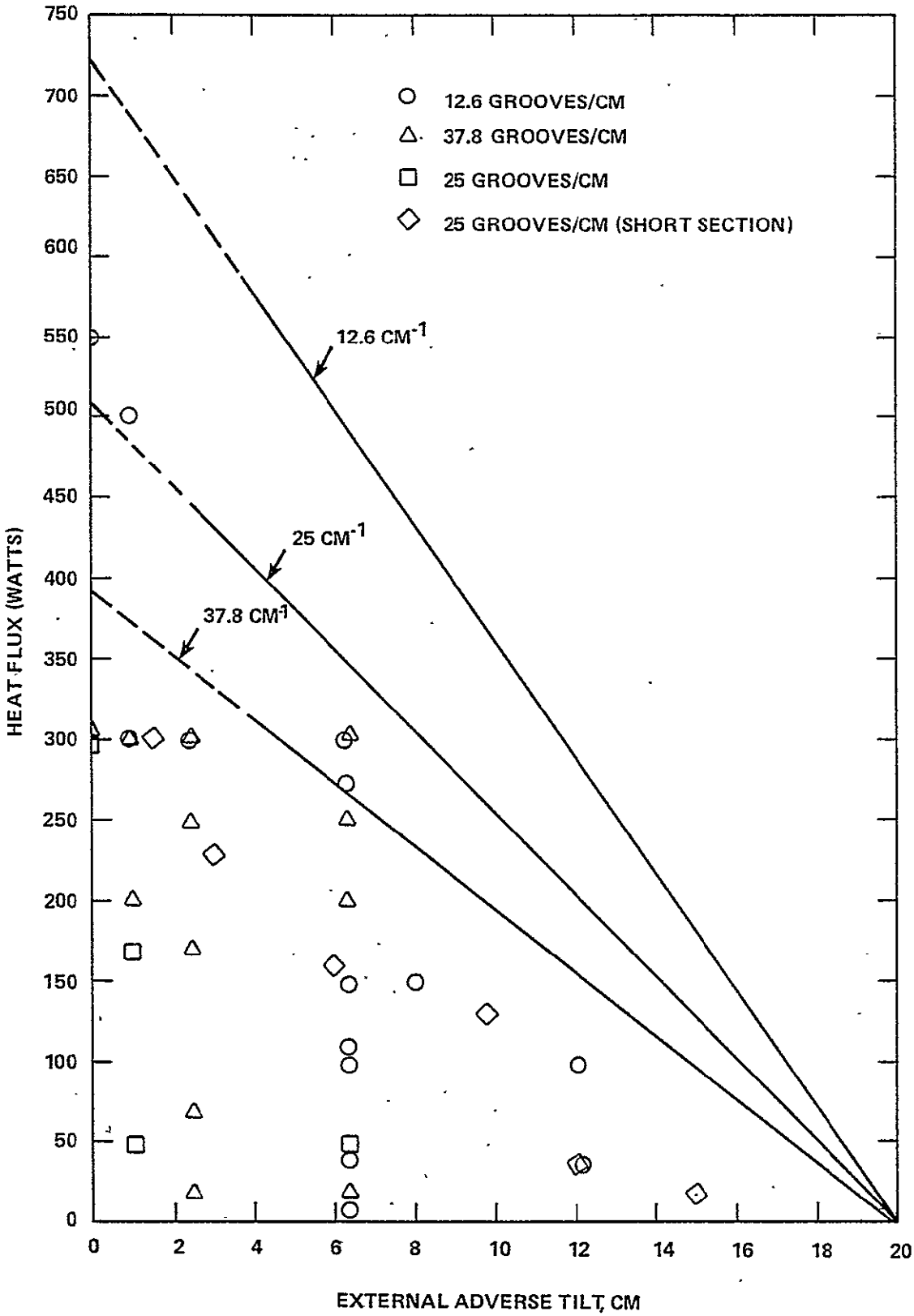

FIGURE 3-5. PREDICTED CAPACITIES FOR THE THREE EVAPORATIVE HEAT TRANSFER SYSTEMS, INCLUDING VAPOR MICROCHANNEL PRESSURE DROPS

7705-124.17

4.0 EXPERIMENTAL RESULTS

The heat pipe evaporators were operated at a number of heat fluxes and elevations to characterize response to heat flux density and liquid/vapor pressure differential. In this report, only the results from the 12.7/cm and 37.8/cm tests will be discussed in detail. Tests performed on the 25/cm surface are discussed in earlier reports.[8,12] Figure 4.1 presents typical data of evaporator temperature difference versus heat flux for the 12.6 and 37.8 groove/cm surfaces at an adverse evaporator-condenser elevation of 6.4 cm. At a heat flux density of 10 W/cm^2, for example, the evaporator temperature drops are about 5.8^{o} and $7.7^{o}C$, respectively, for 37.8 and 12.6 grooves/cm. Two distinct series of tests are shown for the 37.8/cm surface, and they demonstrate the importance of maintaining adequate groove-to-wick cover contact. The data shown with open faced triangular symbols was taken with an evaporator that had an estimated 0.002 to 0.004 cm diametrical clearance between the screen-covered mandrel and the grooved inner diameter. When this was changed to a diametrical interference fit of 0.002 to 0.004 cm, the data shown as solid-faced triangles were obtained. At high heat fluxes, the tight-fitting wick displayed significantly lower evaporator temperature differences, and it is assumed that the liquid film was prevented from receding into the screen, as was possible with the loose-fitting system.

Figure 4.2 presents experimental data on heat transfer coefficients for the 12.7/cm and 37.8/cm surfaces measured as a function of heat flux density under conditions ranging from reflux (-0.25 cm external tilt) to 6.4 cm adverse elevation and from a heat flux density of 0.3 W/cm^2 to 20 W/cm^2. In all cases, the heat transfer coefficient is based on the internal diameter and length of the screw thread zone and on the average evaporator temperature as determined by the 12 evaporator thermocouples. Table 4.1 presents previous experimental data for the 25/cm surface in tabular form.

Although there were significant variations in behavior related to heat pipe tilt and groove density, several generalizations can be made. First, at high adverse tilt both surfaces displayed a cube root dependence of heat transfer coefficient on heat flux density. A least-squares power law fit to data between 0.5 W/cm^2 and 20 W/cm^2 results in

TABLE 4-1. SUMMARY OF PREVIOUS HEAT TRANSFER MEASUREMENTS ON A 25/CM INVERTED MENISCUS SURFACE

Heat Flux Density (W/cm^2)	Heat Transfer Coefficient (W/cm^2K)	Vapor Core Temperature (^oC)	External Tilt (cm)
1.33505	1.05122	19.35	0.0
1.33513	0.890088	19.1	
2.64488	1.3704	20.2	
3.9878	1.7414	21.3	
5.92633	1.8934	22.7	
10.3716	2.81074	26	
1.33063	0.65227	19.7	1.46
2.63774	0.912712	21.05	
3.98101	1.36805	22.4	
5.92053	1.85016	24.1	
8.37155	3.17104	25.4	
10.3221	3.05386	27.2	
12.599	2.83124	29.3	
15.2481	2.65184	31.9	
20.0585	2.66735	36.5	
1.3317	0.752371	19.7	3.0
1.33114	0.735439	19.8	
2.63809	0.995506	21.2	
3.98026	1.42152	22.7	
5.91701	1.60353	24.5	
8.36851	2.52825	25.5	
8.36629	2.02084	26.9	
10.3191	2.76651	27.6	
10.353	2.03001	29.3	
12.5968	2.62434	29.5	
15.2458	2.57531	32.3	
20.0585	2.66735	36.5	

TABLE 4-1 (Continued)

Heat Flux Density (W/cm^2)	Heat Transfer Coefficient (W/cm^2K)	Vapor Core Temperature (^oC)	External Tilt (cm)
1.33083	0.74348	19.9	6.10
2.63737	1.00281	21.4	
3.97853	1.30873	22.9	
5.91283	1.7386	25.8	
8.36321	1.93593	27.5	
10.3488	1.93075	30.1	
1.33229	0.938232	19.9	9.30
2.63971	1.29398	21.4	
3.98042	1.55485	22.9	
1.33146	0.870236	20.0	12.1
2.63857	1.18321	21.5	
1.33051	0.751702	20.0	15.1

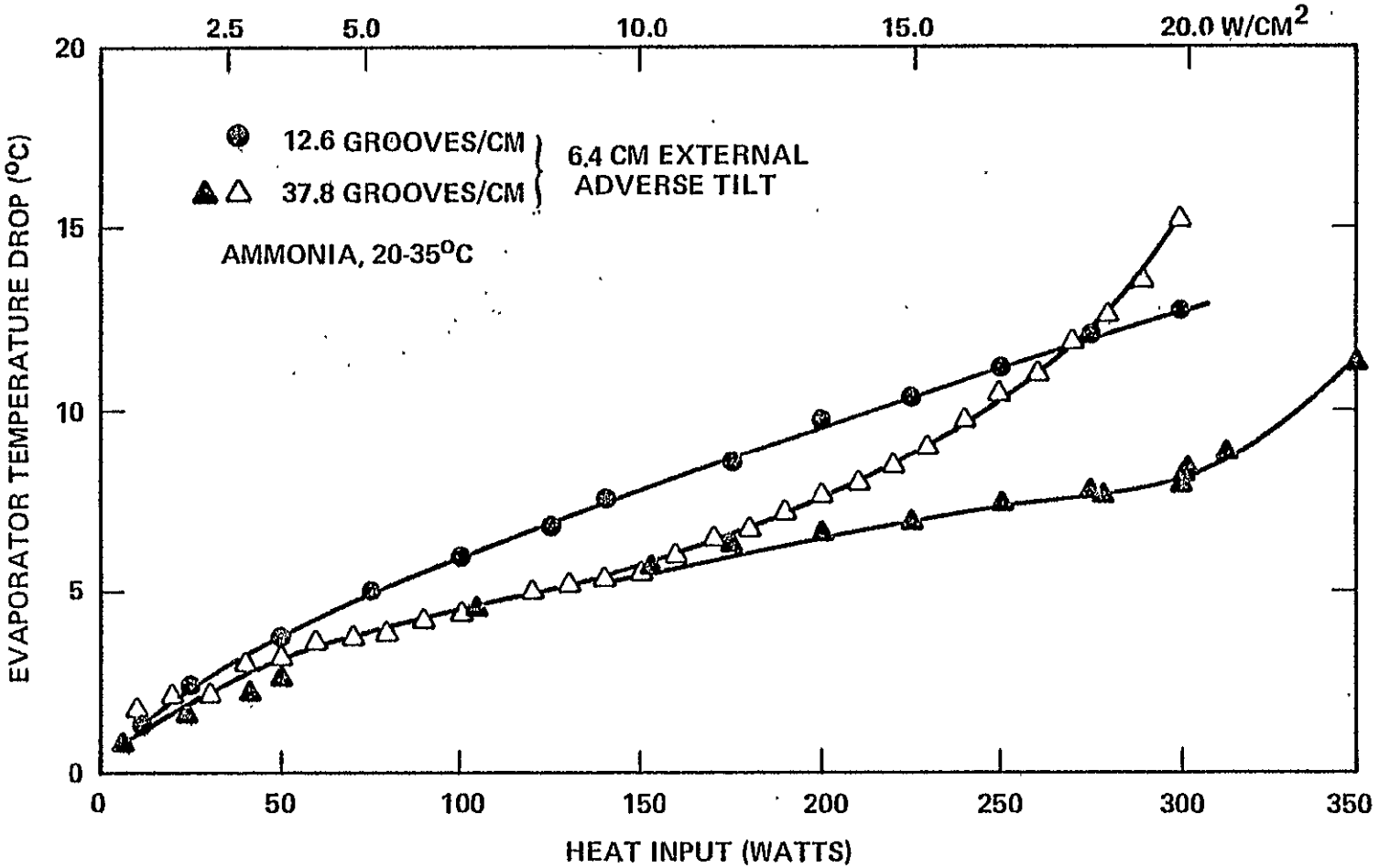

FIGURE 4-1. REPRESENTATIVE INVERTED MENISCUS HEAT TRANSFER BEHAVIOR

7705-124.12

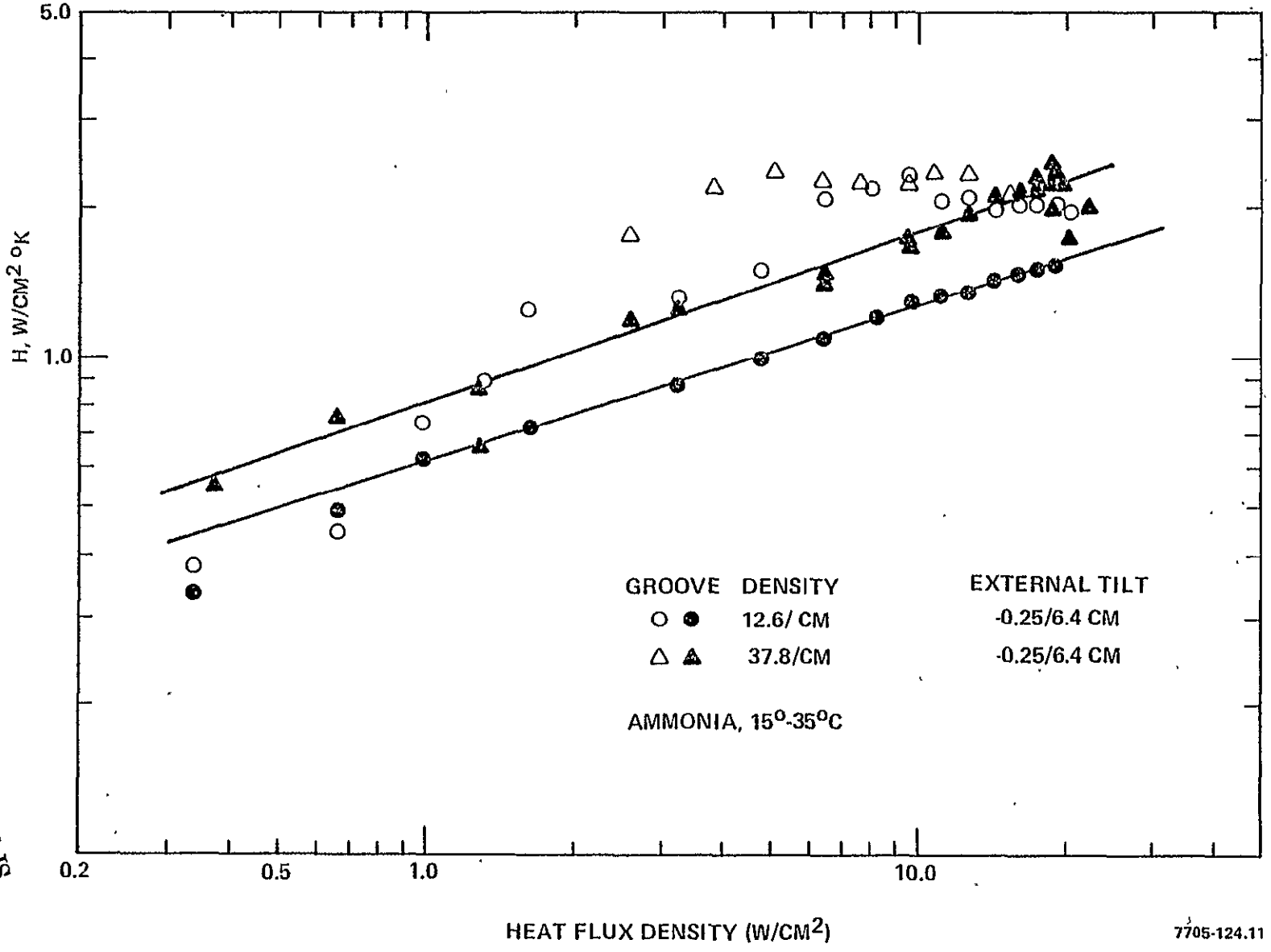

FIGURE 4-2. MEASURED HEAT TRANSFER COEFFICIENTS FOR SCREEN COVERED GROOVES WITH AMMONIA WORKING FLUID

$$H = 0.593\ q_a^{0.325}$$

and

$$H = 0.821\ q_a^{0.344} \qquad (W/cm^2K) \qquad (4\text{-}1)$$

where q_a is the surface heat flux density in W/cm^2, and the equations are respectively for 12.6/cm and 37.8/cm surface groove densities.

Second, both surfaces were operable up to heat flux densities in excess of 20 W/cm^2. At 20 W/cm^2, the film temperature drops were about 12.7°C (H = 1.57 W/cm^2K) and 8.7°C (H = 2.3 W/cm^2K) for groove densities of 12.6/cm and 37.8/cm. Third, both surfaces showed heat transfer coefficients from 1 to 2.5 W/cm^2K under refluxing conditions. Under adverse tilt conditions, the 25/cm inverted meniscus surface shows the characteristic increase in heat transfer coefficient with heat flux density up to about 8 W/cm^2. At this point, the heat transfer coefficient began to gradually decrease. The peak heat transfer coefficient ranged from 2 to a maximum of 3.2, with a higher heat transfer coefficient being observed at lower adverse tilts. The 25/cm inverted meniscus surface displayed the highest heat transfer coefficient, but it may be more directly related to the semicircular groove shape than to an optimum groove density.

A summary of heat transfer results is given in Table 4-2, along with corresponding data for open-groove operation with the 25/cm surface. This table shows that the covering of circumferential grooves with a capillary wick material increased the maximum heat flux density by a factor of 5 to 7 and the heat transfer coefficient by a factor of three to four for the same thread density. The 12.6/cm capillary wick-covered surface also outperformed the 25/cm uncovered grooves. At the 4 W/cm^2 maximum heat flux attained with the open-faced 25/cm surface, the 12.6/cm inverted meniscus surface has demonstrated a heat transfer coefficient of 0.9 to 1.0 W/cm^2K in comparison to only 0.44 to 0.79 W/cm^2K for the 25/cm open groove evaporator.

TABLE 4.2. SUMMARY OF HEAT TRANSFER RESULTS

Parameter	Value			
Groove density, cm^{-1}	12.6	25	25	37.8
Surface type(1)	IV	IV	OG	IV
Groove shape	65^{o} V-shape	cup-shape	cup-shape	66^{o} V-groove
Heat transfer coefficient, W/cm^2K(2)	1.57	2 to 3	0.44 to 0.79	2.35
Maximum heat flux density, W/cm^2	30	20	4	20
Maximum prime height, cm	--	15	6.8	--
Vapor core temperature range, ^{o}C	15-35	20-40	20-40	15-35

(1) IV = inverted meniscus, OG = open groove

(2) These are values at 20 W/cm^2 - refer to Figure 4-2 for variation with heat flux density.

5.0 DATA INTERPRETATION

It has been found that wick-covered grooves display relatively high heat transfer coefficients and high surface heat flux capabilities compared to conventional screw-thread grooves, and that the heat transfer coefficient furthermore increases as the cube root of heat flux density. The overall heat transfer coefficient has also been found to vary slowly with thread density, so that it is possible to design evaporators with relatively coarse threads and yet maintain satisfactory heat transfer characteristics. A factor of 3 increase in groove density results in approximately a 40% increase in heat transfer coefficient . If the dependence of heat transfer coefficient on groove density is assumed to follow a power law, the proprotionality relationship is approximately

$$H \alpha N^{0.32} \qquad (5\text{-}1)$$

where N is the linear groove density. This behavior is at variance with established models of meniscus heat transfer, since the major fraction of heat is generally considered to pass through a relatively abbreviated zone at the fillet tip, hence a doubling of groove density should result in a corresponding factor of two increase in overall heat transfer coefficient.

It has not been possible to definitively establish the heat transfer mechanisms responsible for the performance characteristics of the inverted meniscus surface, but several factors indicate that nucleate boiling may play an important role.

In Figure 5.1, heat transfer behavior for the inverted meniscus is compared with the 25°C pool boiling correlation of Fritz[2] and the -33°C boiling data of Grottzman, et al.[13] The latter data is for the Union Carbide high flux porous boiling surface. The inverted meniscus data very nearly parallels the pool boiling curve and the data of Grottzman, et al. Both boiling relations follow approximately a 1/4-root dependence of "H" on heat flux density. At a given heat flux density, the two wick-covered grooved surfaces

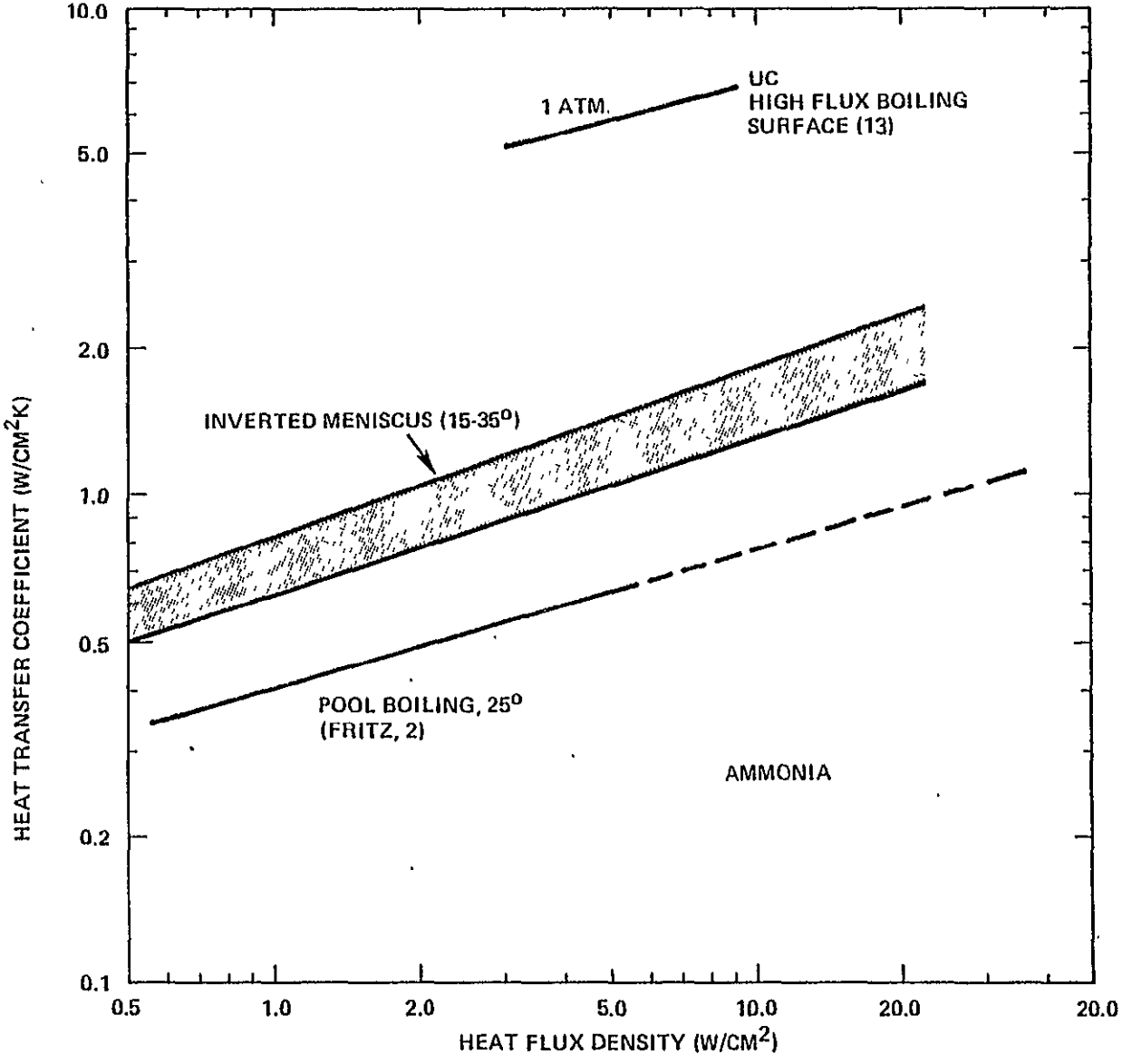

FIGURE 5-1. A COMPARISON OF INVERTED MENISCUS HEAT TRANSFER WITH BOILING HEAT TRANSFER

7705-124.2

respectively show a constant 56% and 220% performance increase relative to pool boiling, but a reduction of about 80% relative to the highly effective porous boiling surfaces. Together, the data of Fritz and Grottzman show that significant changes can be made in surface structure and operating pressure without influencing the functional dependence of boiling heat transfer coefficient on heat flux density, and that the inverted meniscus surface has a functional dependence very similar to pool boiling.

Liquid Film Boiling

If boiling occurs during operation of the inverted meniscus surface, then certain criteria must be met to assure that vapor bubbles will propagate from nucleation sites located under the liquid fillets. Since the spiral grooves in the existing surfaces were machine cut, it is probable that the grooved surfaces contain a large population of potential nucleation sites of varying radius. The problem is complicated to a degree because the liquid film is not constant in thickness and the groove wall beneath the film is not constant in temperature. At the fillet tip, the liquid film is very thin, and the wall temperature is depressed because of constriction resistance. Near the root of the fillet, the heat transfer will be a minimum and the groove wall temperature will approach the exterior evaporator wall temperature, T_{we}. The thick liquid film and high wall temperature at the meniscus root are both conducive to boiling initiation.

To activate a nucleation site, the temperature field in the liquid film must allow the vapor bubble to form a hemispherical shape. Bergles and Rohsenow[14] have developed a model for the prediction of incipient flow boiling that may be used here to estimate the critical nucleation radius for meniscus boiling. The physical situation is shown in Figure 5-2. If the temperature profile in the liquid film is linear and the film surface is in saturated equilibrium with the vapor phase, then it is postulated that boiling will be initiated when the local saturated vapor pressure at $y = r_{ni}$ exactly compensates for the surface tension pressure $2\sigma/r_{ni}$. The radius r_{ni} corresponds to the smallest cavity that can propagate vapor bubbles. Vapor bubbles at sites

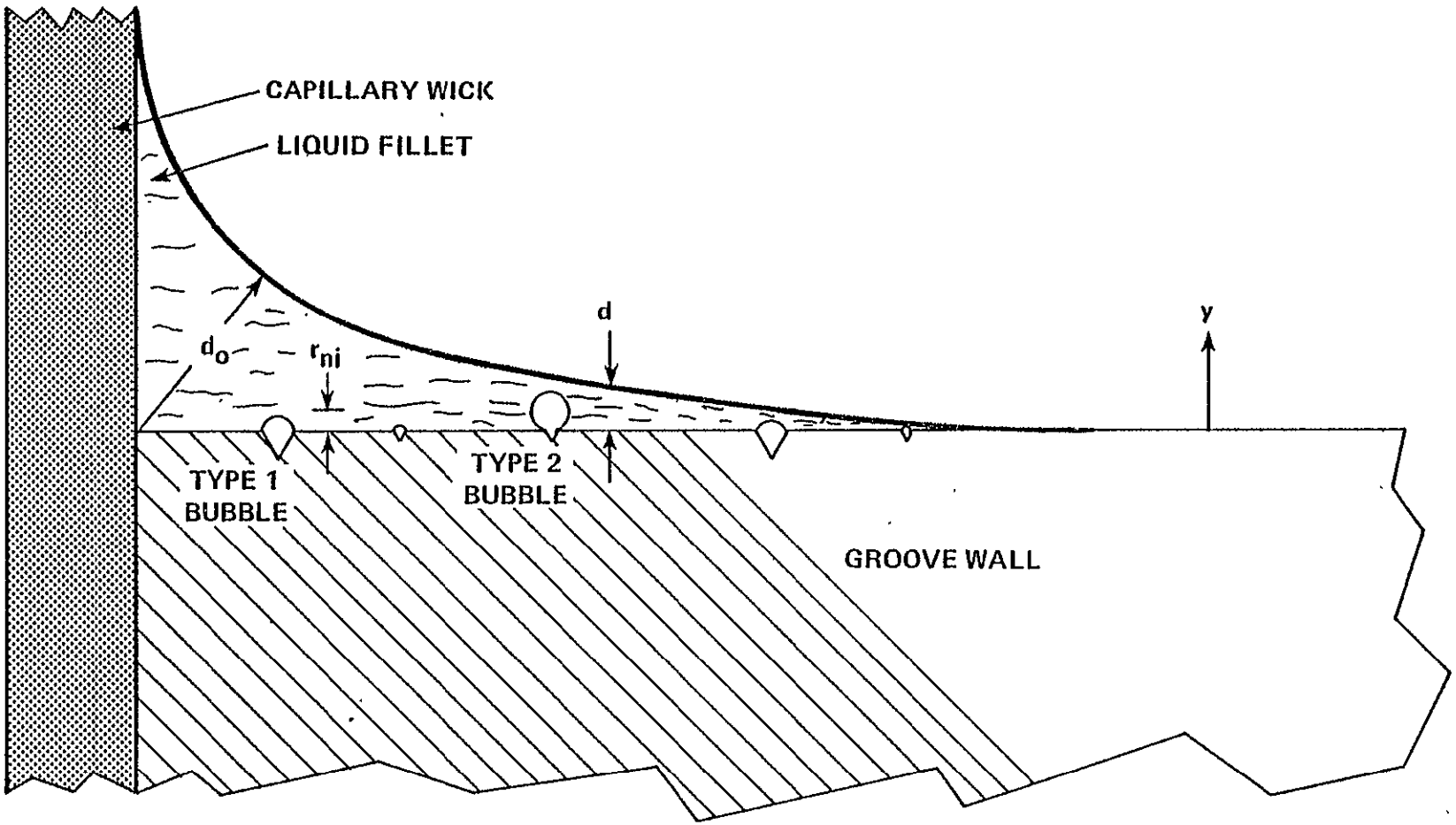

FIGURE 5-2. LIQUID MENISCUS DIMENSIONS RELATED TO INITIATION OF BOILING

with radii greater than r_{ni} will spontaneously grow, whereas bubbles at sites with a smaller radius will not grow in size. That is, larger bubbles do not encounter any unfavorable ratio of surface tension pressure to differential vapor pressure. This criteria does not in itself guarantee boiling will occur, since this depends on the size distribution of nucleation sites and the conditions within each site. Rather, boiling could occur for sites having a radius greater than r_{ni}. It will be shown that this criteria for boiling applies to thin films if r_{ni} is small compared to the film thickness.

For a small film temperature drop, the vapor pressure rise above saturated film conditions at $y = r_{ni}$ can be obtained from the differential form of the Clausius-Clapeyron equation,

$$P_{sr} - P_{vs} = \frac{h_{fg}}{T_{vs} v_{fg}} (T_{\ell r} - T_{vs}) \qquad (5\text{-}2)$$

In the absence of noncondensables, this vapor pressure rise must be greater than or equal to the pressure required to maintain the bubble radius. The pressure rise within the bubble must be (referring to Figures 2.4-1 and 5-1)

$$P_b - P_{vs} = -\frac{\sigma}{r} + \frac{2\sigma}{r_{ni}} \qquad (5\text{-}3)$$

where r is the meniscus local radius of curvature.

The ratio of expression 5-2 to 5-3 is the ratio of available differential vapor pressure to surface tension pressure. If $T_{\ell r}$ is obtained from the assumed linear temperature profile, this ratio is

$$P+ = \frac{P_{sr} - P_{vs}}{P_b - P_{vs}} = \left(\frac{1}{\phi}\right) \cdot \frac{r_b (1 - r_b/d)}{2 - r_b/r} \qquad (5\text{-}4)$$

where $$\phi = \frac{\sigma T_{vs} v_{fg}}{h_{fg} (T_w - T_{vs})} \qquad (5\text{-}5)$$

It can be shown that the two pressure differences are equal for critical radii of

$$r_{ni} = \frac{d}{2}\left[1 \pm \sqrt{1 - \frac{8\phi_{ni}/d}{(1 + \phi_{ni}/r)^2}}\right]\left(1 + \phi_{ni}/r\right) \qquad (5\text{-}6)$$

For most room temperature organic and inorganic working fluids the factor ϕ is quite small, and the characteristic roots represent either a nucleation radius $r_{ni} \ll d$ or a value slightly less than d. For example, the factor at $25^{o}C$ for ammonia, with a $1^{o}C$ wall superheat, is approximately 6.6×10^{-5} cm. This also means that the factor ϕ/r can be neglected for a fillet radius greater than or equal to approximately 10^{-4} cm. A fillet radius of this magnitude may be present near the meniscus tip, but certainly not at the meniscus root for typical heat pipe wick materials. Therefore, the terms containing r may be set to zero.

If a hemispherical vapor bubble of radius r_{ni} is generated at the liquid-metal interface, this bubble must grow in size and depart the surface for boiling to be truly initiated. If the hemispherical bubble cap is considered to be a "Type One" geometry, and the larger bubbles shown in Figure 5.2 to be "Type Two" geometries, then the bubble will definitely grow if the pressure ratio P^{+} at the bubble cap is always greater than or equal to 1.0. Neglecting the influence of r , the pressure ratio P^{+} for the Type Two geometry is

$$P^{+} = \frac{1}{2\phi} \cdot r_b \left[1 - r_b/d\ (1+\alpha)\right] \qquad (5\text{-}7a)$$

where $\alpha = \sqrt{1 - \left(\frac{r_{ni}}{r_b}\right)^2}$; (5-7b)

and where r_{ni} is given by the smaller root of equation 5-6, with ϕ_{ni}/r set to zero. If the ratio p+ is calculated as a function of r_b and r_{ni}, it is found that for $r_{ni}/d \leq 0.17$, the Type One hemispherical cap bubble will spontaneously grow into a Type Two bubble. In contrast, for $r_{ni} \geq 0.17$, the final bubble height equals the initial radius; that is, $y_f = r_{ni}$. Figure 5.3 shows the final size of the bubble, y_f/d, as a function of r_{ni}/d.

It is worthwhile to note that with this model for incipient nucleate boiling, the vapor bubble never actually penetrates the surface. However, it can be assumed that a 90% to 95% penetration is adequate to breach the film, since it can be expected that the actual vapor pressure within the bubble is somewhat higher than the characteristic pressure at its extreme tip. Therefore, for $r_{ni}/d \leq 0.05$, Figure 5.3 shows that the critical state for boiling initiation is the production of a Type 1 bubble cap, and the relation between nucleation site radius and wall superheat at this critical condition is

$$\phi_{ni} = r_{ni}\left(1 - \frac{r_{ni}}{d}\right) \qquad \begin{matrix}\text{(boiling initiation} \\ \text{when } r_{ni} \leq 0.05\ d)\end{matrix} \qquad (5\text{-}8)$$

For nucleation site radii greater than 0.05 d, additional superheat is needed to attain a 90% to 95% film penetration. If the superheat factor necessary to form a bubble of height $y = \beta d$ is denoted ϕ_{yf}, then the ratio of ϕ_{ni} to ϕ_{yf} is, for constant film thickness,

$$\frac{\phi_{ni}}{\phi_{yf}} = \frac{r^+_{ni}\,(1 - r^+_{ni})}{\beta\left(1 - \beta\left[1 + \sqrt{1 - (r^+_{ni}/\beta)^2}\right]\right)} \qquad (5\text{-}9)$$

where $r^+_{ni} = r_{ni}/d$.

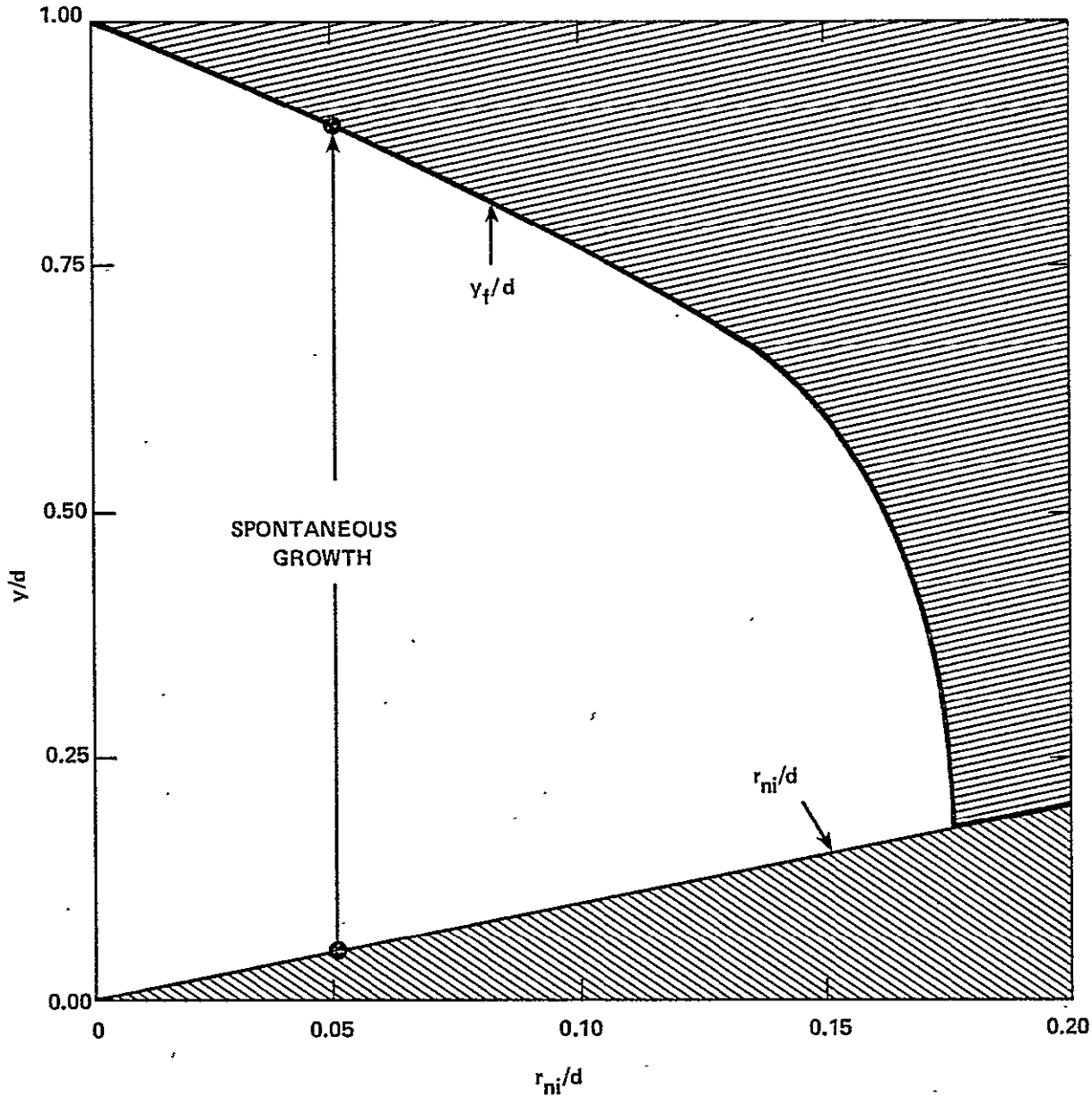

FIGURE 5-3. THE EQUILIBRIUM SIZE FOR AN INITIALLY HEMISPHERICAL VAPOR BUBBLE OF RADIUS r_{ni}, SHOWING THE GROWTH PHENOMENA CHARACTERISTIC OF NUCLEATION AT SMALL SITES

7705-124.14

This ratio is presented in Figure 5-4 for β = 0.50, 0.75, 0.90, and 0.95. As an example, for a bubble that initially in Type 1 condition spans 20% of the film thickness (r^+_{ni} = 0.20), growth of the bubble requires additional wall superheat as follows.

For y_f =	0.5 d;	ϕ_{ni}/ϕ_{yf} = 1.1
=	0.75 d;	= 1.6
=	0.90 d;	= 3.4
=	0.95 d;	= 6.4

At a constant film thickness, a hemispherical bubble that is initially 20% of the thickness will require the wall-to-vapor temperature difference to increase by a factor of 3.4 to enlarge the bubble to 90% of the film depth. In the particular case of ammonia at 25°C, let r_{ni} = 2.5 (10^{-4}) cm, and d = 1.25 (10^{-3}) cm. The superheat corresponding to the initial condition is 0.33°C, while for y_f = 0.9 d, the superheat required is 1.1°C. Although this analysis is necessarily approximate, it indicates that vapor bubbles can be produced within the liquid fillets in a grooved or inverted meniscus heat pipe at relatively low wall superheats, and that the bubbles may be quasi-stable over certain heat flux ranges. These stable bubbles could lead to enhanced heat transfer through capillary jet phenomena.[15]

For the "H" versus q data gathered in this experimental program, the incipient nucleation radii can be calculated at each condition using the equation

$$r^+_{ni} = \frac{1}{2}\left(1 - \sqrt{1 - \frac{8\,\sigma\, v_{fg}\, T_{vs}\, H}{d \cdot h_{fg}\, q_a}}\right) \qquad (r^+_{ni} < 0.05) \qquad (5\text{-}10)$$

To establish for the present work the nucleation site radii that might be activitated, and the heat fluxes necessary, the characteristic film thickness d appearing in Equation 5-10, has been set equal to the dimension d_o of Figure 5-2. This value is approximately 1.32 x 10^{-3} cm. Predicted values of $2r_{ni}$ are presented in Figure 5-5.

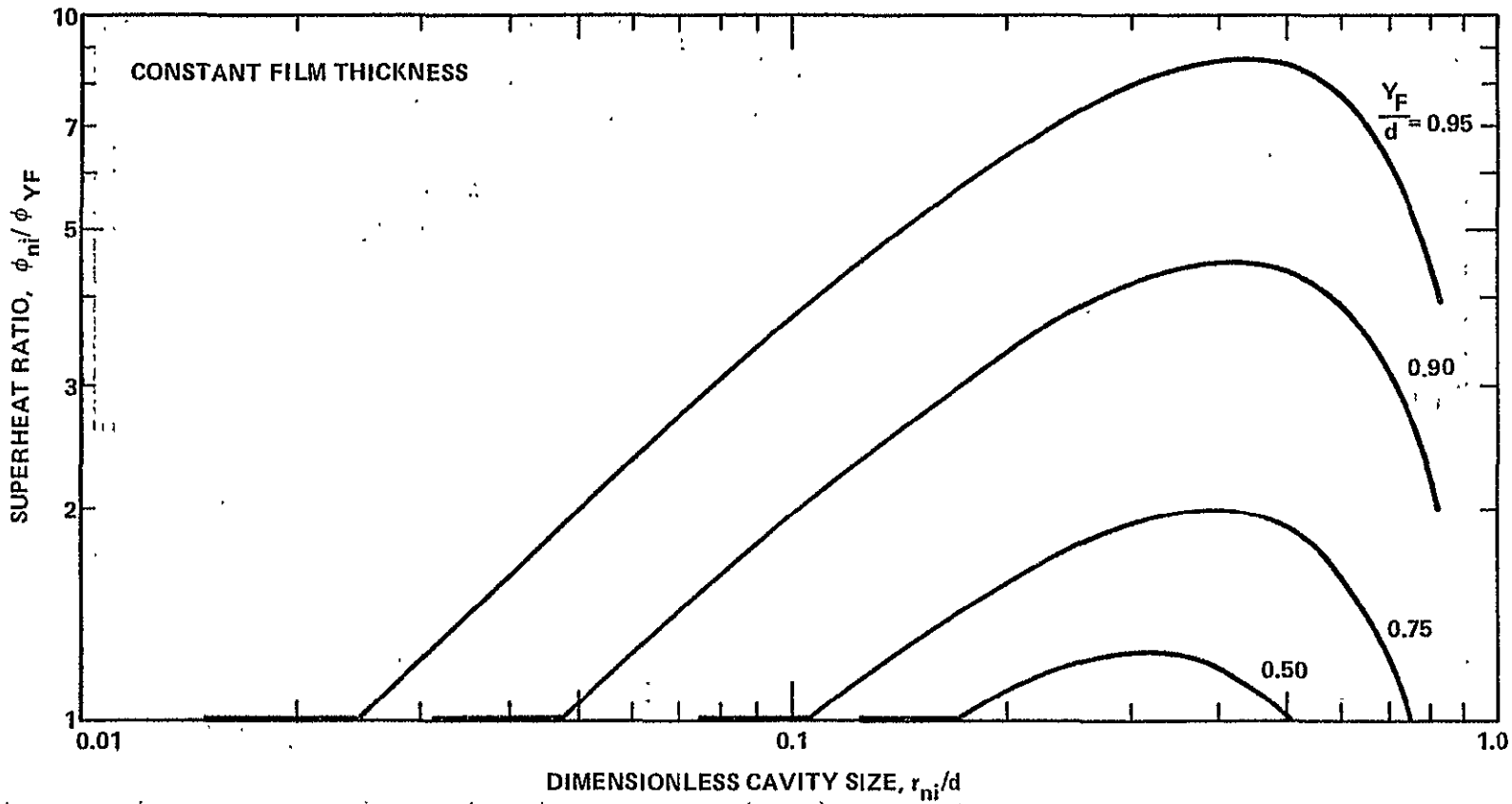

FIGURE 5–4. THE ADDITIONAL SUPERHEAT REQUIRED TO FORM A VAPOR BUBBLE OF HEIGHT Y_F FROM A HEMISPHERICAL BUBBLE CAP OF RADIUS r_{ni}

7705-181.

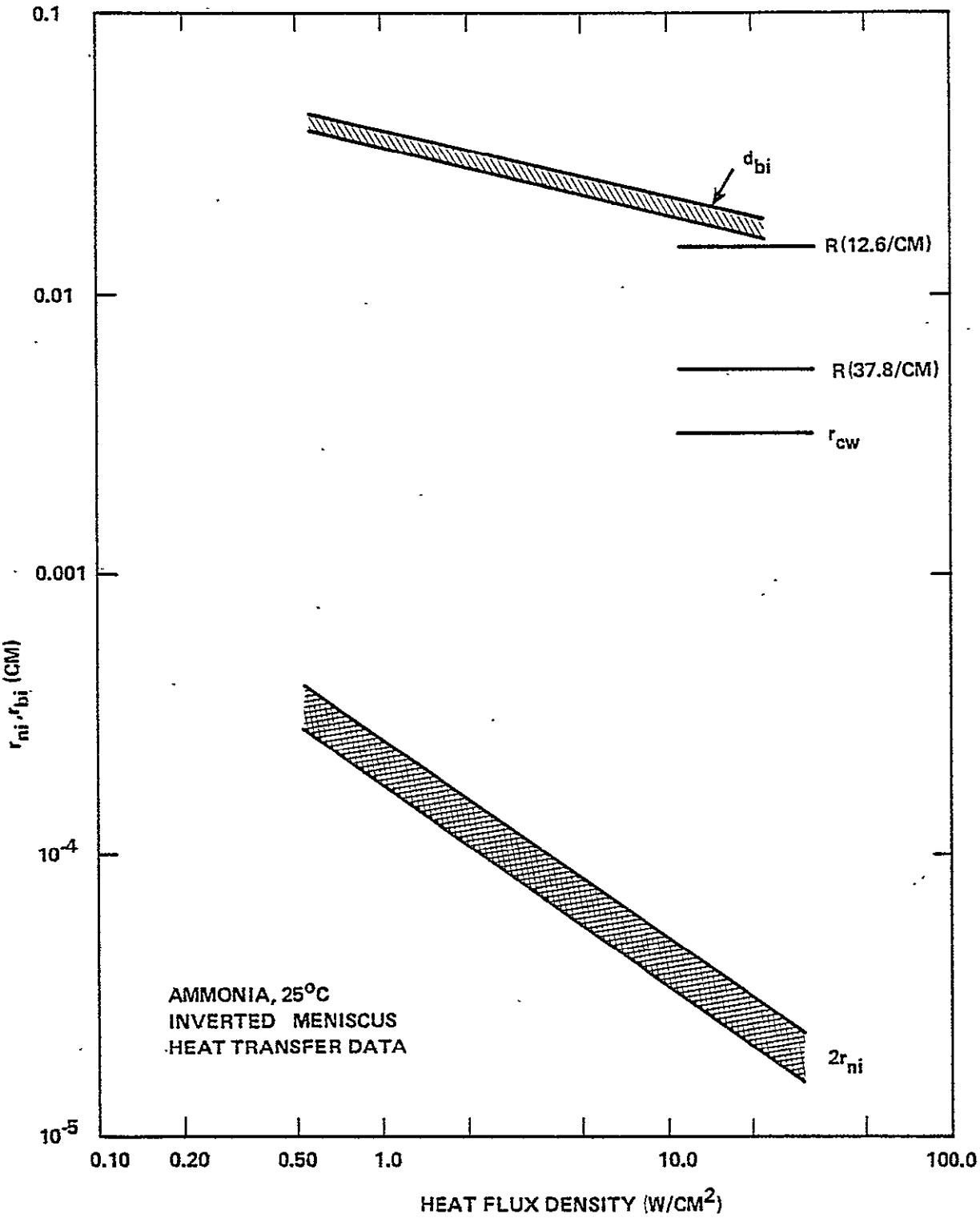

FIGURE 5-5. THE MINIMUM PORE RADIUS (r_{ni}) FOR INCIPIENT BOILING, AND THE CORRESPONDING VAPOR BUBBLE DEPARTURE RADIUS, r_{bi}

7705-124.13

For most machined surfaces, nucleation sites range in size from 10^{-5} cm to 10^{-3} cm. These calculations indicate that all incipient nucleation site diameters fall between 3×10^{-5} cm and 3×10^{-4} cm, which is well within the range of observed nucleation site sizes.

Vapor Bubble Departure Radius

For spacecraft applications it is important to determine if nucleate boiling characteristics in a thin, surface tension dominated liquid meniscus will change in going from 1g to zero g conditions. One of the most fundamental differences would be the possible formation of discrete vapor bubbles in 1g only, as a result of interacting surface tension and bouyancy forces. The departure radius for a vapor bubble is given by the approximate transcendental formula[16]

$$r_{bi}^3 \cong \frac{3}{2} \cdot \frac{\sigma r_{ni}}{g(\rho_\ell - \rho_v)} \cdot \left[1 - 0.381\left(\frac{r_{ni}}{r_{bi}}\right)^{0.451}\right] \qquad r_{bi} \geq r_{ni} \qquad (5\text{-}11)$$

Figure 5-5 shows the critical nucleation diameter and corresponding bubble departure diameter for the "H" versus q_a data of Figure 4-2. The bubble departure diameters fall in the range 1.5 (10^{-2}) to 4 (10^{-2}) cm, and are much larger than the characteristic film thickness, d_o, which is 1.32 (10^{-3}) cm. Since the lift-off diameters based on bouyancy exceed the film thickness, it can be expected that gravity will play a minor role in any meniscus boiling phenomena, and that zero-g and 1-g performance should be very similar.

6.0 SUMMARY

Inverted meniscus surfaces of 12.6/cm and 37.8/cm V-groove density have been operated to heat flux densities in excess of 20 W/cm^2 with ammonia. At 20 W/cm^2, the respective heat transfer coefficients were 1.57 W/cm^2K and 2.3 W/cm^2K, while at lower heat flux densities, the overall evaporative heat transfer coefficient varied as the cube root of heat flux. If the heat transfer coefficient is assumed to follow a power law dependence on groove density, then the power is +0.32. That is, the heat transfer coefficient changes very slowly with variations in groove density, and the inverted meniscus is of particular interest in that relatively high heat transfer coefficients and very high heat flux densities have been demonstrated for low groove densities.

The approximate cube root dependencies on heat flux and groove density are unlike the dependencies normally expected for grooved evaporative surfaces, where the heat transfer coefficient is assumed to be linear in groove density and relatively independent of heat flux. Instead, the surfaces show behavior similar to pool boiling.

Pool boiling heat transfer coefficients for ammonia follow an approximate fourth-root dependence on heat flux density under diverse surface conditions. Furthermore, calculations show that conditions are favorable for initiation of thin-film boiling within the liquid fillets for a wide range of heat flux densities. These calculations further imply that nucleate boiling may be present in open groove evaporators as well as in inverted meniscus evaporators, and that the bubbles produced may influence both heat transfer and fluid transport.

To gain a fundamental understanding of fillet evaporation, heat transfer models for grooved surfaces were developed. Two-dimensional conduction models for rectangular grooves showed that thermal constriction resistance in each metal tooth is a negligible factor in restricting evaporation of ammonia for rectangular grooved metal surfaces constructed of high conductivity metals

such as aluminum. With low conductivity metals such as stainless steel, however, this resistance could be quite significant.

A composite model for evaporation from rectangular grooves was also developed that includes one-dimensional conduction heat transfer in the metal tooth and liquid fillet, and an approximate solution to the Navier Stokes equation for liquid flow within the fillet. In the past, investigators have modeled meniscus heat transfer as a pure two-dimensional conduction problem. The present analysis indicates that liquid flow from the base of a fillet to the tip can create a significant liquid pressure drop parallel to the groove wall, and that this liquid pressure change can strongly influence fillet shape and thermal resistance. These calculations suggest that the modeling and optimization of grooved surfaces for evaporative heat transfer may require consideration not only of conduction processes, but also of fluid transport processes within the liquid menisci.

7.0 REFERENCES

1. R. Kosson, et al., AIAA Paper 72-273, AIAA Thermophysics Conference, San Antonio, Texas, April 10, 1972.

2. W. Fritz, Chem. Ingr. Tech., Vol. 35: 753, 1963.

3. R. Siegel and C. Usiskin, J. Ht. Trans., Trans. ASME, Vol. 81: 3, 1959.

4. K. Feldman and M. Berger, Tech. Rpt. ME-62(73)ORN-012-2, Office of Naval Research Contract N00014-68-A-0155, Sept. 1973.

5. D. Edwards, et al., ASME Paper 73-HT-25, ASME-AICHE Heat Transfer Conference, Atlanta, Ga., August 5, 1973.

6. G. Schneider and M. Yovanovich, AIAA Paper 76-481, AIAA 11th Thermophysics Conference, San Diego, Ca., July 14, 1976.

7. Personal communication with R. Cary, Micro Extrusions, 2871 LaMesa, Anaheim, Ca.

8. E. Saaski, NASA Report CR 137,724, August 1975.

9. K. Feldman, NASA Report CR 137,912, UNM Tech. Rpt. ME-70(76)NASA-365-1, July 1976.

10. K. Schlitt, J. Kirkpatrick, and P. Brennan, Paper 74-724, AIAA/ASME 1974 Thermophysics and Heat Transfer Conference, Boston, Mass., 1974.

11. G. Johnson and E. Saaski, 1972 ASME Winter Annual Meeting, ASME Paper 72-WA/HT-36.

12. E. Saaski and J. Franklin, A High Performance Evaporative Heat Transfer Wick, National Heat Transfer Conference, St. Louis, Mo., August 1976.

13. C. F. Grottzman, et al., Field Experience with High Efficiency Heat Exchangers, AICHE 74th National Meeting, New Orleans, La., March 12, 1973.

14. A. Bergeles and W. Rohsenow, Jnl. of Ht. Trans., Trans. of ASME, p. 365, August 1964.

15. B. K. Larkin, AIChE J., Vol. 16: 101, 1970.

16. A. Adamson, Physical Chemistry of Surfaces, Interscience Publishers, New York, N.Y., 1967.